Journal of Geophysical Research: Atmospheres

RESEARCH ARTICLE
10.1029/2017JD027970

This article is a companion to Vadas and Becker (2018) https://doi.org/10.1029/2017JD027974.

Key Points:
- Secondary GWs create fishbone structures in z-t plots and have the same periods, wavelengths, and azimuths above and below the knee
- Polarization relations and broad spectra cause the temperature and vertical velocity spectra to peak at different periods and wavelengths
- Secondary GWs with 6- to 10-hr periods and 6- to 14-km vertical wavelengths are identified in fishbone structures at $z = 43-52$ km in McMurdo lidar data

Correspondence to:
S. L. Vadas and X. Chu,
vasha@nwra.com;
xinzhao.chu@colorado.edu

Citation:
Vadas, S. L., Zhao, J., Chu, X., & Becker, E. (2018). The excitation of secondary gravity waves from local body forces: Theory and observation. *Journal of Geophysical Research: Atmospheres*, *123*, 9296–9325. https://doi.org/10.1029/2017JD027970

Received 30 OCT 2017
Accepted 29 MAR 2018
Accepted article online 23 MAY 2018
Published online 12 SEP 2018

©2018. American Geophysical Union. All Rights Reserved.

The Excitation of Secondary Gravity Waves From Local Body Forces: Theory and Observation

Sharon L. Vadas[1], **Jian Zhao**[2], **Xinzhao Chu**[2], **and Erich Becker**[3]

[1]Northwest Research Associates, Boulder, Colorado, USA, [2]Cooperative Institute for Research in Environmental Sciences and Department of Aerospace Engineering Sciences, University of Colorado Boulder, Boulder, CO, USA, [3]Leibniz Institute of Atmospheric Physics, Kühlungsborn, Germany

Abstract We examine the characteristics of secondary gravity waves (GWs) excited by a localized (in space) and intermittent (in time) body force in the atmosphere. This force is a horizontal acceleration of the background flow created when primary GWs dissipate and deposit their momentum on spatial and temporal scales of the wave packet. A broad spectrum of secondary GWs is excited with horizontal scales much larger than that of the primary GW. The polarization relations cause the temperature spectrum of the secondary GWs generally to peak at larger intrinsic periods τ_{Ir} and horizontal wavelengths λ_H than the vertical velocity spectrum. We find that the one-dimensional spectra (with regard to frequency or wave number) follow lognormal distributions. We show that secondary GWs can be identified by a horizontally displaced observer as "fishbone" or ">" structures in $z-t$ plots whereby the positive and negative GW phase lines meet at the "knee," z_{knee}, which is the altitude of the force center. We present two wintertime cases of lidar temperature measurements at McMurdo, Antarctica (166.69°E, 77.84°S) whereby fishbone structures are seen with $z_{\text{knee}} = 43$ and 52 km. We determine the GW parameters and density-weighted amplitudes for each. We show that these parameters are similar below and above z_{knee}. We verify that the GWs with upward (downward) phase progression are downward (upward) propagating via use of model background winds. We conclude that these GWs are likely secondary GWs having ground-based periods $\tau_r = 6-10$ hr and vertical wavelengths $\lambda_z = 6-14$ km, and that they likely propagate primarily southward.

1. Introduction

In a stably stratified atmosphere, there are only two types of internal, linear waves in addition to quasi-geostrophic and large-scale equatorial waves: atmospheric gravity waves (GWs) and acoustic waves (AWs) (Hines, 1960). Although AWs can be powerful tracers for phenomena like earthquakes or tsunamis, they typically carry very little energy and momentum and so do not contribute substantially to the dynamical control of the middle atmosphere. This is because typical meteorological processes (such as the wind flow over mountains, updrafts within deep convection, and breakdown of weather vortices) have wind speeds that are much less than the sound speed. GWs generated from these processes have much larger amplitudes and therefore account for most of the vertical transport of energy and momentum from the troposphere to the middle atmosphere. Additional vertical transport arises from Rossby waves and thermal tides.

Because the "amplitude" of a GW grows nearly exponentially with altitude as $\sim \exp(z/2\mathcal{H})$, where $\mathcal{H}$ is the density scale height, a GW can have important effects at higher altitudes even if its initial amplitude is small. Here a GW's amplitude is u', v', w', $\rho'/\bar{\rho}$, and $T'/\bar{T}$, where u', v', and w' are the GW zonal, meridional, and vertical velocity perturbations, respectively, ρ' and T' are the density and temperature perturbations, respectively, and $\bar{\rho}$ and $\bar{T}$ are the background density and temperature, respectively. Important GW damping processes at higher altitudes include (Fritts & Alexander, 2003) the following:

1. A primary GW reaches a critical level and dissipates when $\omega_{Ir} \to 0$ and $\lambda_z \to 0$, where ω_{Ir} is the intrinsic frequency;
2. A primary GW breaks when it approaches the condition of convective instability, that is, when $|u'_H/(c_H - U_H)| \simeq 0.7-1.0$. Here $u'_H = \sqrt{(u')^2 + (v')^2}$, $c_H = \omega_r/k_H$ is the horizontal phase speed, $\omega_r = 2\pi/\tau_r$ is the ground-based frequency, $k_H = \sqrt{k^2 + l^2} = 2\pi/\lambda_H$, λ_H is the horizontal wavelength, k, l, and m are the zonal,

meridional, and vertical wave numbers, respectively,

$$U_H = (k\bar{U} + l\bar{V})/k_H \quad (1)$$

is the background horizontal wind along the direction of GW propagation, and $\bar{U}$ and $\bar{V}$ are the zonal and meridional components of the background wind, respectively, and

$$\omega_{Ir} = \omega_r - (k\bar{U} + l\bar{V}) = \omega_r - k_H U_H. \quad (2)$$

Both of these processes are highly nonlinear and result in (1) the cascade of energy and momentum to smaller scales and (2) the eventual transition to turbulence. Additionally, small-scale secondary GWs are excited. These secondary GWs have λ_H and $|\lambda_z|$ smaller than those of the primary GWs and have small horizontal phase speeds of up to tens of meters per second (e.g., Bacmeister & Schoeberl, 1989; Bossert et al., 2017; Chun & Kim, 2008; Franke & Robinson, 1999; Satomura & Sato, 1999; Zhou et al., 2002). Because these small-scale secondary GWs often cannot propagate very far before being reabsorbed into the fluid (although they may carry and transport significant momentum flux in the process; Bossert et al., 2017), they can be loosely thought of as being part of the transition to turbulence. Because of their small horizontal phase speeds, those small-scale secondary GWs that propagate to $z \sim 105$ km will dissipate rapidly near the turbopause from molecular viscosity and thermal diffusivity (Vadas, 2007).

During the transition to turbulence, momentum and energy are deposited into the mean flow. Because the spatial region over which this deposition occurs is of order a few times the spatial extent of the primary GW packet, and because the time scale over which this occurs is of order a few times the temporal extent of the primary GW packet, this deposition occurs on the order of the spatial and temporal scales of the breaking primary GW packet. This deposition results in a localized (in space and time) horizontal acceleration of the mean (background) flow, dubbed a "local body force" (Fritts et al., 2006; Vadas & Fritts, 2001, 2002; Vadas et al., 2003). Here "local body" refers to the fact that this force is localized in space and time with respect to the mean flow. This body force accelerates the background flow in the direction of propagation of the primary GWs, causing the flow to be unbalanced. The fluid responds by (1) creating a 3-D mean flow that consists of two counter-rotating cells (Vadas & Liu, 2009) and (2) exciting larger-scale secondary GWs which propagate upward and downward, and forward and backward away from the force (Vadas et al., 2003). In an idealized atmosphere (i.e., isothermal and constant wind in z and t), 50% of the secondary GWs propagate upward (downward), and 50% propagate forward (backward) away from the body force (Vadas et al., 2003). Although these secondary GWs propagate in all azimuths except perpendicular to the body force direction, they have the largest amplitudes parallel and antiparallel to the force direction. On horizontal slices in an idealized atmosphere, these secondary GWs appear as partial concentric rings and form identical forward and backward GW momentum flux "headlights." Although the amplitudes of the downward propagating secondary GWs decrease rapidly in z, the amplitudes of the upward propagating secondary GWs increase rapidly as $\sim \exp(z/2\mathcal{H})$, thereby suggesting that they could greatly affect the variability and dynamics of the atmosphere at higher altitudes.

It is important to note that these latter secondary GWs (created from body forces) are quite different from the former secondary GWs (created from small-scale nonlinearities that occur during GW breaking). The momentum flux spectrum of these latter secondary GWs peaks at $\lambda_H \simeq 2\mathcal{D}_H$ and $\lambda_z \simeq \mathcal{D}_z$ to $2\mathcal{D}_z$, where $\mathcal{D}_H$ and $\mathcal{D}_z$ are the full width and full depth of the body force, respectively, and $\mathcal{D}_H$ ($\mathcal{D}_z$) is several times the width (depth) of the dissipating wave packet (Vadas & Fritts, 2001; Vadas et al., 2003). In particular, these secondary GWs have much larger λ_H than that of the primary GWs in the wave packet. For example, if a breaking primary GW packet with horizontal wavelength λ_H contains two wave cycles, then the region over which wave breaking occurs is $2\lambda_H$. Once the transition to turbulence has occurred, the region where momentum has been deposited into the fluid is approximately twice the width of the breaking GW packet (Vadas & Fritts, 2002). This is represented mathematically in the formula for the body force via the spatial smoothing of the GW momentum fluxes (see section 2). Therefore, we estimate that the full width of the body force is $\mathcal{D}_H \simeq 4\lambda_H$ for this example. This results in a dominant horizontal wavelength of the secondary GWs of $\sim 8\lambda_H$, because the secondary GW spectrum peaks at $\lambda_H \sim 2\mathcal{D}_H$ (see above). Thus, the horizontal wavelength for the secondary GWs excited by a body force are much larger than that of the primary breaking GWs that created this force. In this paper, we investigate these latter secondary GWs because they have the potential to significantly influence the dynamics of the atmosphere at much higher altitudes due to their larger phase speeds and vertical wavelengths (Vadas, 2007).

Using the high-resolution, GW-resolving Kühlungsborn Mechanistic general Circulation Model (KMCM) (Becker, 2009, 2017; Becker et al., 2015), Becker and Vadas (2018) recently examined the GW processes which occur during strong mountain wave (MW) events in the southern winter polar region. They found that the dissipation of MWs in the stratopause region resulted in body forces with average amplitudes of ~1,000 m/s/day over the southern Andes, and ~700 m/s/day over McMurdo. These forces excited larger-scale secondary GWs having both zonal and meridional momentum fluxes. During large events, these secondary GWs had large temperature perturbations of $T' \sim 15-30$ K in the mesopause region over McMurdo. Additionally, the dissipation of some of these secondary GWs at $z \sim 90-100$ km created an additional eastward maximum of the mean zonal wind at ~60°S, thus affecting the mean circulation. Since the simulated and observed temperature perturbations agreed well over McMurdo (see Figure 14 of that work), Becker and Vadas (2018) concluded that the mean flow effects of secondary GWs are likely quite important in the real atmosphere.

In this paper, we use theory and observations to more closely examine secondary GWs from body forces. In section 2, we review the compressible analytic solutions for the excitation of secondary GWs from intermittent, localized body forces. In section 3, we examine the secondary GW spectra excited by idealized body forces in the stratosphere and show how the temperature and velocity spectra differ. We also show how the secondary GWs can be identified by ground-based observers via "fishbone" structures in *z*-*t* plots. We analyze two cases where fishbone structures are seen in the wintertime lidar temperature data at McMurdo Station in section 4. Our conclusions and a discussion are contained in section 5.

2. Compressible Analytic Solutions for the Excitation of Secondary GWs and Mean Responses From Localized, Intermittent Horizontal Body Forces

In this section, we review the *f* plane, compressible analytic solutions that describe the secondary GWs excited by a localized (in space) and intermittent (in time) horizontal body force. The *f* plane, Boussinesq analytic solutions were derived by Vadas and Fritts (2001, 2013). Vadas (2013) generalized these solutions to include compressibility and found that the inclusion of compressibility is necessary to accurately determine the amplitudes of the secondary GWs having λ_z larger than one to two times $\pi\mathcal{H}$. Here we review the compressible solutions because $|\lambda_z|$ can exceed the Boussinesq limit.

If a GW packet dissipates, momentum is deposited into the fluid on spatial and temporal scales on the order of the scales of the wave packet (Fritts et al., 2006; Vadas & Fritts, 2002). This momentum deposition creates a local body force which causes the background flow to accelerate horizontally in the direction of propagation of the GW packet. We assume that λ_H of the GW is much smaller than the horizontal scale of the background flow (e.g., tides and planetary waves). The zonal and meridional components of the local body force (i.e., the localized acceleration of the background flow) are given by the convergence of the pseudo momentum flux (Appendix A of Vadas & Becker, 2018):

$$F_{x,\mathrm{tot}} = -\frac{1}{\bar{\rho}}\partial_z\left(\bar{\rho}\left(\overline{u'w'} - \frac{f\,C_p}{g}\overline{T'v'}\right)\right), \quad F_{y,\mathrm{tot}} = -\frac{1}{\bar{\rho}}\partial_z\left(\bar{\rho}\left(\overline{v'w'} + \frac{f\,C_p}{g}\overline{T'u'}\right)\right). \tag{3}$$

Here u, v, and w are the zonal, meridional, and vertical velocities, respectively, ρ is density, and T is temperature. The primes denote deviations from the background flow due to GWs, and overlines denote averages over several GW wavelengths. Additionally, g is the gravitational acceleration, C_p is the mean specific heat capacity at constant pressure, and f is the Coriolis parameter in the *f* plane approximation, that is, $f = 2\Omega\sin\Theta$ with $\Omega = 2\pi/24$ hr and Θ being a fixed latitude. The heat flux terms in equation (3) correspond to the Stokes drift correction for atmospheric waves that are affected by the Coriolis force (Dunkerton, 1978). Note that equation (3) is equivalent to the corresponding expression given in Fritts and Alexander(2003, equation(41)) when using the polarization relations for a monochromatic GW. In the limit that $f = 0$, equation (3) reduces to the familiar expression involving the convergence of the Reynolds stress tensor.

Although nonlinear small-scale dynamics is part of the wave breaking process, we only focus here on the linear effects that the resulting body force has on scales comparable to or larger than the scales of the body force. The evolution of the flow is then described by the following equations:

$$\frac{D\mathbf{v}}{Dt} + \frac{1}{\rho}\nabla p - g\mathbf{e}_z + f\,\mathbf{e}_z \times \mathbf{v} = \mathbf{F}(\mathbf{x})\mathcal{F}(t), \tag{4}$$

$$\frac{D\rho}{Dt} + \rho\nabla.\mathbf{v} = 0, \tag{5}$$

$$\frac{DT}{Dt} + (\gamma - 1)T\nabla.\mathbf{v} = 0. \tag{6}$$

Here $D/Dt = \partial/\partial t + (\mathbf{v}.\nabla)$, $\mathbf{v} = (u, v, w)$ is the velocity vector, p is pressure, and $\mathbf{e}_z$ is the unit vector in the vertical direction. We use the ideal gas law, $p = r\rho T$, where $r = 8,308/X_{MW}$ m^2 s^{-2} K^{-1}, X_{MW} is the mean molecular weight of the particle in the gas (in g/mol), $\gamma - 1 = r/C_v$, and C_v is the mean specific heat at constant volume.

The spatial portion of the body force is $\mathbf{F}(\mathbf{x}) = (F_x(\mathbf{x}), F_y(\mathbf{x}), 0)$. The total zonal and meridional components of the body force are

$$F_{x,\text{tot}} = F_x(\mathbf{x})\mathcal{F}(t), \quad F_{y,\text{tot}} = F_y(\mathbf{x})\mathcal{F}(t), \tag{7}$$

respectively, where the temporal dependence is given by the analytic function $\mathcal{F}(t)$. Note that F_x and F_y can be any continuous and derivable functions of $\mathbf{x}$. Also note that we neglect the effect of the energy deposition in equation (6).

We expand the flow variables as contributions from (1) the background flow (denoted with overlines) plus (2) perturbations from the secondary GWs *and* from the induced mean responses (e.g., counterrotating cells) (the perturbations are denoted with primes):

$$\begin{aligned} u &= \bar{U} + u', \quad & v &= \bar{V} + v', \quad & w &= w', \\ \rho &= \bar{\rho} + \rho', \quad & T &= \bar{T} + T', \quad & p &= \bar{p} + p'. \end{aligned} \tag{8}$$

We emphasize that u', for example, contains the zonal wind perturbations from the secondary GWs plus the zonal wind perturbations from the counterrotating cells in the induced mean response. In order to derive the mean responses and excited secondary GW spectrum, we assume that $\bar{T}$, X_{MW}, and γ are constant, implying

$$\bar{\rho} = \bar{\rho}_0 e^{-z/\mathcal{H}}, \tag{9}$$

where $\bar{\rho}_0$ is the background density at $z = 0$ and $\mathcal{H} = r\bar{T}/g$ is the (constant) density scale height. We further make the simplifying assumption that $\bar{U}$ and $\bar{V}$ constant. (Nevertheless, the resulting GW spectrum can be ray traced through a varying background atmosphere, as has been done previously (e.g., Vadas & Liu, 2009, 2013; Vadas, 2013; Vadas et al., 2014). We linearize equations (4)–(6) then solve these equations for the following smooth (but finite duration) temporal function of the body force:

$$\mathcal{F}(t) = \frac{1}{\chi}\begin{cases} (1 - \cos\hat{a}t) & \text{for } 0 \le t \le \chi \\ 0 & \text{for } t \le 0 \text{ and } t \ge \chi. \end{cases} \tag{10}$$

Here $\mathcal{F}$ has duration χ and frequency $\hat{a}$,

$$\hat{a} \equiv 2\pi n/\chi, \tag{11}$$

where the number of cycles is $n = 1, 2, 3, \ldots$. Following Vadas (2013), we define the following variables and scaled horizontal force components as

$$\begin{aligned} &\xi = e^{-z/2\mathcal{H}}u', \quad \sigma = e^{-z/2\mathcal{H}}v', \quad \eta = e^{-z/2\mathcal{H}}w', \\ &\phi = e^{z/2\mathcal{H}}\rho'/\bar{\rho}_0 = e^{-z/2\mathcal{H}}\rho'/\bar{\rho}, \quad \psi = e^{z/2\mathcal{H}}p'/\bar{\rho}_0 = e^{-z/2\mathcal{H}}p'/\bar{\rho}, \\ &\zeta = e^{-z/2\mathcal{H}}T'/\bar{T}_0, \quad F_{xs} = e^{-z/2\mathcal{H}}F_x, \quad F_{ys} = e^{-z/2\mathcal{H}}F_y. \end{aligned} \tag{12}$$

We expand ξ, σ, η, ϕ, ψ, ζ, F_{xs}, and F_{ys} in a Fourier series:

$$\xi(x, y, z, t) = \frac{1}{(2\pi)^3}\int_{-\infty}^{\infty}\int_{-\infty}^{\infty}\int_{-\infty}^{\infty} e^{-i(kx+ly+mz)}\widetilde{\xi}(k, l, m, t)\mathrm{d}k\,\mathrm{d}l\,\mathrm{d}m, \tag{13}$$

where "~" denotes the Fourier transform of the variable and $\mathbf{k} = (k, l, m)$ is the wave vector. We then take the Laplace transform of the equations (Abramowitz & Stegun, 1972) and solve them algebraically. After the force is finished (i.e., when $t \geq \chi$), the mean and GW solutions are (equations(45)–(49) of Vadas, 2013, with all AW terms set to 0):

$$\widetilde{\xi}_{FH}(t) = \frac{i\hat{a}^2 l}{f}K + \frac{i\hat{a}^2}{\chi\left(f^2-\omega_1^2\right)}\left[(kO+lfP)\mathcal{C}(\omega_1) + \left(-k\omega_1 P + \frac{lfO}{\omega_1}\right)\mathcal{S}(\omega_1)\right], \tag{14}$$

$$\widetilde{\sigma}_{FH}(t) = -\frac{i\hat{a}^2 k}{f}K + \frac{i\hat{a}^2}{\chi\left(f^2-\omega_1^2\right)}\left[(lO-kfP)\mathcal{C}(\omega_1) - \left(l\omega_1 P + \frac{kfO}{\omega_1}\right)\mathcal{S}(\omega_1)\right], \tag{15}$$

$$\widetilde{\eta}_{FH}(t) = \frac{\hat{a}^2(i\gamma\mathcal{H}m_s - 1)}{\chi\gamma\mathcal{H}\left(N_B^2-\omega_1^2\right)}\left[O\mathcal{C}(\omega_1) - P\omega_1\mathcal{S}(\omega_1)\right], \tag{16}$$

$$\widetilde{\phi}_{FH}(t) = \frac{im_s g(\gamma-1)\hat{a}^2}{c_s^2 N_B^2}K + \frac{\hat{a}^2}{\chi c_s^2}\left(\frac{im_s g(\gamma-1)-\omega_1^2}{N_B^2-\omega_1^2}\right)\left[\frac{O}{\omega_1}\mathcal{S}(\omega_1) + P\mathcal{C}(\omega_1)\right], \tag{17}$$

$$\widetilde{\psi}_{FH}(t) = \hat{a}^2 K + \frac{\hat{a}^2}{\chi}\left[\frac{O}{\omega_1}\mathcal{S}(\omega_1) + P\mathcal{C}(\omega_1)\right], \tag{18}$$

where $m_s = m - i/2\mathcal{H}$

$$\mathcal{S}(\omega) = \sin\omega t - \sin\omega(t-\chi), \tag{19}$$

$$\mathcal{C}(\omega) = \cos\omega t - \cos\omega(t-\chi), \tag{20}$$

$$A_F = k\widetilde{F_{xs}} + l\widetilde{F_{ys}}, \tag{21}$$

$$B_F = k\widetilde{F_{ys}} - l\widetilde{F_{xs}}, \tag{22}$$

$$K = \frac{f}{\hat{a}^2 s_1^2 s_2^2}\left(ic_s^2 B_F N_B^2\right), \tag{23}$$

$$O = \frac{1}{s_1^2\left(s_2^2-s_1^2\right)\left(\hat{a}^2+s_1^2\right)}\left(-ic_s^2 f B_F\left(N_B^2+s_1^2\right)\right), \tag{24}$$

$$P = \frac{1}{s_1^2\left(s_2^2-s_1^2\right)\left(\hat{a}^2+s_1^2\right)}\left(-ic_s^2 A_F\left(N_B^2+s_1^2\right)\right). \tag{25}$$

Since $p'/\bar{p} = \rho'/\bar{\rho} + T'/\bar{T}$ from the ideal gas law, the scaled temperature perturbation is

$$\widetilde{\zeta} = \frac{\gamma}{c_s^2}\widetilde{\psi} - \widetilde{\phi}. \tag{26}$$

Here $N_B = \sqrt{(\gamma-1)g^2/c_s^2}$ is the buoyancy frequency and $c_s = \sqrt{\gamma g\mathcal{H}}$ is the sound speed. Additionally, the GW intrinsic frequency is $\omega_{GW} = \omega_1 = -is_1$ and the AW intrinsic frequency is $\omega_{AW} = \omega_2 = -is_2$; both satisfy the same dispersion relation:

$$\omega_{Ir}^4 - \left[f^2 + c_s^2(\mathbf{k}^2 + 1/4\mathcal{H}^2)\right]\omega_{Ir}^2 + c_s^2\left[k_H^2 N_B^2 + f^2(m^2+1/4\mathcal{H}^2)\right] = 0, \tag{27}$$

which has solutions

$$s_1^2 = -\omega_1^2 = -\frac{a}{2}\left[1 - \sqrt{1-4b/a^2}\right], \tag{28}$$

$$s_2^2 = -\omega_2^2 = -\frac{a}{2}\left[1 + \sqrt{1-4b/a^2}\right], \tag{29}$$

where

$$a = -\left(s_1^2+s_2^2\right) = \left[f^2 + c_s^2(\mathbf{k}^2+1/4\mathcal{H}^2)\right], \tag{30}$$

$$b = s_1^2 s_2^2 = c_s^2\left[k_H^2 N_B^2 + f^2(m^2+1/4\mathcal{H}^2)\right]. \tag{31}$$

Note that equations (14)–(18) include only the compressible GW solutions; the additional branch with acoustic wave (AW) solutions is not included here. Nevertheless, the GW solutions include effects from compressibility. In particular, it is still necessary to calculate the AW frequency $s_2 = i\omega_{AW}$ in order to obtain the GW solutions. Finally, note that there is no limitation on the vertical wavelength, $|\lambda_z|$, relative to the density scale height $\mathcal{H}$.

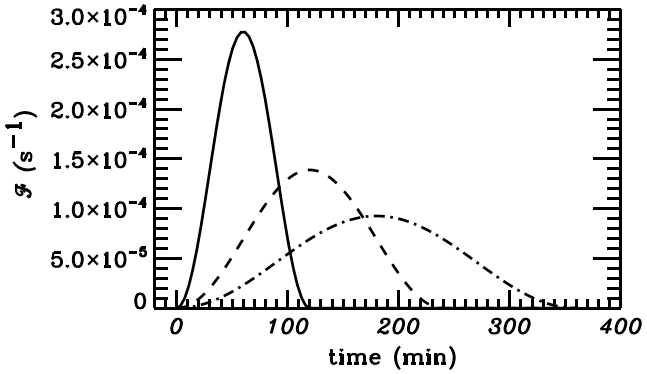

Figure 1. $\mathcal{F}(t)$ (in s^{-1}) for body force durations of $\chi = 2$ (solid), 4 (dashed), and 6 hr (dash-dotted) for $n = 1$.

The square brackets in equations (14)–(18) contain the GW terms; because these terms are proportional to $1/\chi$, no secondary GWs are excited if $\chi \rightarrow \infty$ (i.e., if the momentum deposition takes an infinite amount of time to occur). This is in contrast to the mean terms in equations (14)–(18), which do not depend on χ. These mean terms describe the flow components associated with the counter-rotating cells mentioned in section 1 and discussed in the next section. Importantly, the GW amplitudes are linearly proportional to the body force amplitudes, since the GW terms are proportional to F_{xs} and F_{ys}. If a GW propagates much slower than the sound speed ($\omega_{GW}/\sqrt{\mathbf{k}^2 + 1/4\mathcal{H}^2} \ll c_s$), then $4b/a^2 \ll 1$, and equation (28) becomes $s_1^2 \simeq -b/a$, which is equivalent to the well-known f plane, anelastic GW dispersion relation (Marks & Eckermann, 1995):

$$\omega_{Ir}^2 = {\omega_{GW}}^2 = \frac{k_H^2 N_B^2 + f^2(m^2 + 1/4\mathcal{H}^2)}{\mathbf{k}^2 + 1/4\mathcal{H}^2}. \tag{32}$$

3. Secondary GW Spectra and Mean Responses Created by Horizontal Local Body Forces

In this section, we examine the GW solutions for several idealized, localized, intermittent body forces. These body forces are based on a body force studied in Vadas and Becker (2018) that was created via the breaking of a MW packet with $\lambda_H \sim 230$ km in the stratopause region above McMurdo, Antarctica. These MWs were created on 9.5 July (i.e., 12 UT on 9 July) by a downslope, eastward wind from the Transantarctic Mountains to the west coast of the Ross Sea (Watanabe et al., 2006). This body force excited secondary GWs, which propagated upward and downward from the force, and swept over McMurdo a few hours later, creating a clear fishbone structure in $\sqrt{\bar{\rho}}u'$. As mentioned in section 2, a body force with any horizontal and vertical extents will create secondary GWs as long as its duration is not infinite. Thus, the idealized body force we consider here is only one example of a body force that might occur in the atmosphere. Other body forces would also create secondary GWs having different spectral properties.

We model the secondary GWs by using the analysis of the previous section combined with a zonal body force that is located at (x_0, y_0, z_0) and has the form of a 3-D Gaussian:

$$F_x(\mathbf{x}) = u_0 \exp\left(-\frac{(x-x_0)^2}{2\sigma_x^2} - \frac{(y-y_0)^2}{2\sigma_y^2} - \frac{(z-z_0)^2}{2\sigma_z^2}\right). \tag{33}$$

The full zonal, meridional, and vertical extents of this force are $\mathcal{D}_x = 4.5\sigma_x$, $\mathcal{D}_y = 4.5\sigma_y$, and $\mathcal{D}_z = 4.5\sigma_z$, respectively (Vadas et al., 2003). From equations (7) and (10), the maximum acceleration per unit mass associated with this body force is

$$\frac{2u_0}{\chi}. \tag{34}$$

The studied body force had a full width of $\mathcal{D}_H = \mathcal{D}_x = \mathcal{D}_y \simeq 800$ km, a full depth of $\mathcal{D}_z \simeq 8$ km, and a duration of $\chi < 12$ hr. The force was centered at $z \simeq 46$ km near the stratopause; because this force was created near

the end of a strong MW event and was at a lower altitude, the force amplitude was relatively small: ∼30–50 m/s/day. As mentioned in section 1, Becker and Vadas (2018) found that the body forces at McMurdo on 7.5 July at $z \sim 60$ km had amplitudes that were ∼10–20 times larger: ∼700 m/s/day. Because the secondary GW amplitudes are proportional to the body force amplitude, this would result in secondary GW amplitudes that are ∼10–20 times larger.

Given these parameters, we model a zonal body force with $\mathcal{D}_H = 800$ km and $\mathcal{D}_z = 8$ km (or $\sigma_x = \sigma_y = 180$ km and $\sigma_z = 1.8$ km). We consider several force durations here, in order to see how this duration "cuts off" the highest-frequency portion of the secondary GW spectrum having $\tau_{lr} = 2\pi/\omega_{lr} < \chi$. Figure 1 shows $\mathcal{F}(t)$ with $n = 1$ and $\chi = 2, 4$, and 6 hr. Note that the same amount of momentum is deposited into the fluid in each case. An amplitude of 50 m/s/day is equivalent to 2 m/s/hr, which is $u_0 \simeq 6$ m/s for $\chi = 6$ hr, using equation (34). We choose $u_0 = 5$ m/s here. Because the solutions are linear, the secondary GW amplitudes are proportional to u_0; therefore, it is trivial to scale the solutions to larger u_0 using the results in this section. On the other hand, the GW wavelengths and frequencies are independent of u_0. We locate the body force near the stratopause at $z_0 = 45$ km. (Note that this is a representative altitude of the "knees" of the fishbone structures in the McMurdo lidar data (see section 4).) We also set $n = 1$ and $x_0 = y_0 = 0$.

We place our body force on a "grid" with zonal, meridional, and vertical grid spacings of $\Delta x = 200$ km, $\Delta y = 200$ km, and $\Delta z = 2.2$ km, respectively. We also choose the number of x, y, and z points to be $N_x = 128$, $N_y = 128$, and $N_z = 256$, respectively. Thus, the x, y, and z domain lengths are $L_x = N_x \Delta x = 25,600$ km, $L_y = N_y \Delta y = 25,600$ km, and $L_z = N_z \Delta z = 570$ km, respectively. We also set $\bar{T} = 231$ K, $\mathcal{H} = 6.9$ km, $\gamma = 1.4$, $X_{\rm MW} = 28.9$ g/mole, $\Theta = -70°$, $f = -1.37 \times 10^{-4}$ rad/s, $N_B = 0.02$ rad/s, and $g = 9.65$ m/s^2.

We first show an example of a fast forcing with duration $\chi = 2$ hr. Figure 2a shows the spectrum of the vertical flux of horizontal momentum for the secondary GWs having azimuths (east of north) of 80–100°. Thus, these GWs propagate mainly in the $+x$ direction. Here, the vertical flux of horizontal momentum is

$$2\left(\widetilde{u'_H}\widetilde{w'}^{*}\,\Delta k\,\Delta l\,\Delta m\right)\left(1 - f^2/\omega_{lr}^2\right), \tag{35}$$

where "*" denotes the complex conjugate and

$$\Delta k = \frac{2\pi}{N_x \Delta x}, \quad \Delta l = \frac{2\pi}{N_y \Delta y}, \quad \Delta m = \frac{2\pi}{N_z \Delta z}. \tag{36}$$

Note that the factor $(1 - f^2/\omega_{lr}^2)$ in equation (35) corresponds to the Stokes drift correction for a monochromatic inertia GW. For comparison, Figure 2b shows the corresponding result in the case of the Boussinesq approximation. As expected, the spectra are similar for $|\lambda_z| < 30$ km. Figure 2c shows the fractional relative difference between the compressible and Boussinesq solutions. The relative difference is larger than ∼40% for $\tau_{lr} = 2\pi/\omega_{lr} < 2$ hr and $|\lambda_z| > 30$ km, and for $\tau_{lr} > 3.8$ hr and $|\lambda_z| > 50$ km. The compressible spectrum peaks at approximately twice the body force width, 4–5 times the depth, and 1–2 times the duration: $\lambda_H \sim 1,400$–$2,000$ km, $|\lambda_z| \sim 30$–55 km, and $\tau_{lr} \sim 2$–4 hr.

Figure 3 shows the power spectral density amplitudes of the horizontal velocity, vertical velocity, and relative temperature associated with the compressible secondary GW spectrum shown in Figure 2a:

$$|\widetilde{u'_H}|^2\,\Delta k\,\Delta l\,\Delta m, \quad |\widetilde{w'}|^2 \Delta k\,\Delta l\,\Delta m, \quad |\widetilde{T'}/\bar{T}|^2\,\Delta k\,\Delta l\,\Delta m. \tag{37}$$

Although these spectra represent the *same* secondary GWs, the spectral components peak at very different wavelengths and periods. In particular, the horizontal velocity spectrum peaks at $\lambda_H \sim 1,400$–$3,200$ km, $|\lambda_z| \sim 15$–40 km, and $\tau_{lr} \sim 3$–7 hr, the vertical velocity spectrum peaks at $\lambda_H \sim 1,000$–$1,700$ km, $|\lambda_z| \sim 32$–63 km, and $\tau_{lr} \sim 2$–3.5 hr, and the temperature spectrum peaks at $\lambda_H \sim 1,300$–$2,300$ km, $|\lambda_z| \sim 20$–45 km, and $\tau_{lr} \sim 3$–5.5 hr. Such results mean that a single set of excited secondary GWs will appear to have different peak values if viewed via the horizontal velocity, vertical velocity, or temperature perturbations; as we see next, this is because the secondary GW spectrum is quite broad.

We can understand why these spectra vary so significantly by investigating the f-plane, nondissipative, compressible GW polarization relations. Equations (B8), (B9), and (B11) from Vadas (2013) are

$$\hat{w} = \frac{-\omega_{lr}\left(m - \frac{i}{2\mathcal{H}} + \frac{i}{\gamma\mathcal{H}}\right)\left(\omega_{lr}^2 - f^2\right)(k\omega_{lr} + ifl)}{\left(N_B^2 - \omega_{lr}^2\right)\left(k^2\omega_{lr}^2 + f^2 l^2\right)}\,\hat{u}, \tag{38}$$

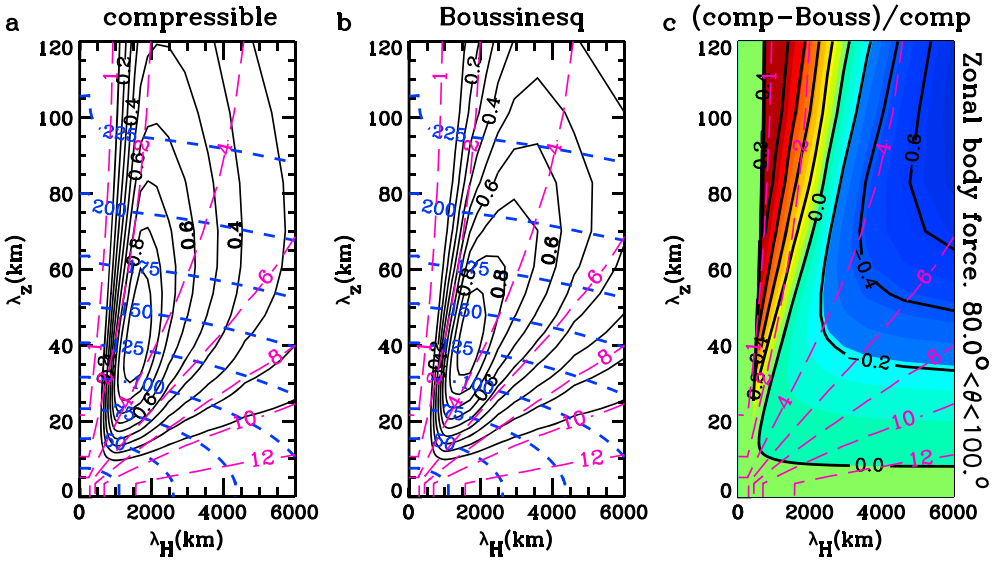

Figure 2. Compressible (a) and Boussinesq (b) vertical flux of horizontal momentum for the secondary gravity waves having azimuths of 80–100° excited by a zonal body force centered at $z_0 = 45$ m with $D_H = 800$ km, $D_z = 8$ km, and $\chi = 2$ hr. Each spectrum is normalized by its maximum value (which is arbitrary) and is shown in 10% increments of its maximum value (solid black lines). Blue short dashed lines indicate the intrinsic horizontal phase speed, c_{IH}, in 25 m/s intervals. (c) (Compressible-Boussinesq)/compressible fluxes from (a) and (b) (solid black lines). Pink long dashed lines show gravity wave intrinsic periods, τ_{Ir}, in hours.

$$\hat{w} = \frac{-\omega_{Ir}\left(m - \frac{i}{2\mathcal{H}} + \frac{i}{\gamma\mathcal{H}}\right)\left(\omega_{Ir}^2 - f^2\right)\left(l\omega_{Ir} - ifk\right)}{\left(N_B^2 - \omega_{Ir}^2\right)\left(l^2\omega_{Ir}^2 + f^2k^2\right)}\,\hat{v}, \tag{39}$$

$$\hat{T} = \frac{N_B^2\left(im - \frac{1}{2\mathcal{H}}\right) - \frac{\omega_{Ir}^2}{\gamma\mathcal{H}}(1-\gamma)}{g\omega_{Ir}\left(m - \frac{i}{2\mathcal{H}} + \frac{i}{\gamma\mathcal{H}}\right)}\,\hat{w}, \tag{40}$$

respectively. Here the "hatted" quantities are

$$\begin{aligned} \hat{u} &= \widetilde{(e^{-z/2\mathcal{H}}u')} = \widetilde{\xi}, \qquad \hat{v} = \widetilde{(e^{-z/2\mathcal{H}}v')} = \widetilde{\sigma}, \\ \hat{w} &= \widetilde{(e^{-z/2\mathcal{H}}w')} = \widetilde{\eta}, \qquad \hat{T} = \widetilde{(e^{-z/2\mathcal{H}}T'/\bar{T})} = \widetilde{\zeta}, \end{aligned} \tag{41}$$

where the widetilde " ~ " encompasses all factors within each parenthesis. We rewrite equations (38) and (39) in terms of the horizontal velocity perturbation via rotating the coordinate system and making the substitutions $u' \to u'_H$, $k \to k_H$ and $l \to 0$. We then obtain

$$\hat{w} = \frac{-\left(m - \frac{i}{2\mathcal{H}} + \frac{i}{\gamma\mathcal{H}}\right)\left(\omega_{Ir}^2 - f^2\right)}{\left(N_B^2 - \omega_{Ir}^2\right)k_H}\,\hat{u}_H, \tag{42}$$

where $\hat{u}_H = \widetilde{(e^{-z/2\mathcal{H}}u'_H)}$. Because the buoyancy period, $\tau_B = 2\pi/N_B$, is $\tau_B \simeq 5.2$ min, we can neglect ω_{Ir}^2 with respect to N_B^2 for midfrequency GWs. Additionally, $|2\pi/f| = 12.28$ hr at McMurdo. As we show in the next figure, we can neglect f if $\tau_{Ir} < 4.5$ hr. For midfrequency GWs with $\tau_B \ll \tau_{Ir} < 4.5$ hr and $|\lambda_z| < 2\pi\mathcal{H}$, equations (40) and (42) become

$$\hat{w} \simeq -\frac{m\omega_{Ir}^2}{k_H N_B^2}\,\hat{u}_H \simeq -\frac{\omega_{Ir}}{N_B}\,\hat{u}_H, \tag{43}$$

$$\hat{T} = \frac{iN_B^2}{g\omega_{Ir}}\hat{w} \simeq -\frac{iN_B^2 k_H}{g\omega_{Ir}m}\,\hat{u}_H \simeq -\frac{iN_B}{g}\,\hat{u}_H, \tag{44}$$

where we have used $\omega_{Ir} \simeq k_H N_B/m$ from equation (32) and $m\hat{w} \simeq k_H\hat{u}_H$ from equation (5) (i.e., $\nabla.\mathbf{v} \simeq 0$). This implies that $u'_H \propto -(1/\omega_{Ir})w'$, $T' \propto (i/\omega_{Ir})w'$, and $T' \propto -iu'_H$ for midfrequency GWs. Therefore, the horizontal

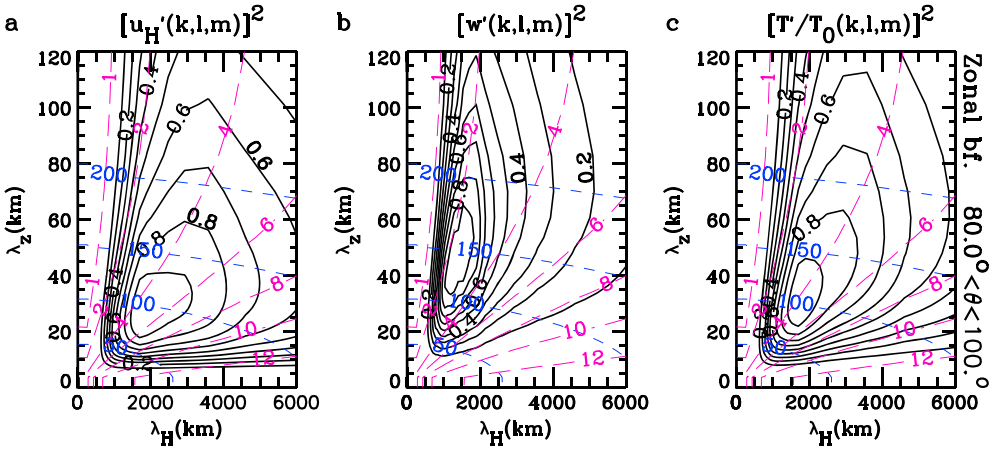

Figure 3. Power spectral density amplitudes, equation (37), of the compressible solutions shown in Figure 2a for the secondary gravity waves having azimuths of 80–100°. (a) Horizontal velocity spectrum: $|\widetilde{u'_H}|^2\ \Delta k\Delta l/\Delta m$. (b) Vertical velocity spectrum: $|\widetilde{w'}|^2\ \Delta k\Delta l/\Delta m$. (c) Temperature perturbation spectrum: $|\widetilde{T'}/\bar{T}|^2\ \Delta k\Delta l/\Delta m$. Each spectrum is normalized by its maximum value (which is arbitrary) and is shown in 10% increments of its maximum value as solid lines. Blue short dashed lines show c_{lH} in 50 m/s increments, and pink long dashed lines show τ_{lr} in hours.

velocity and temperature spectra are weighted by contributions from GWs with smaller intrinsic frequencies, while the vertical velocity spectrum is weighted by contributions from GWs with larger intrinsic frequencies. Importantly, only if a GW spectrum is monochromatic will u'_H, T', and w' peak at the same frequency and wave numbers. Equation (44) also implies that the horizontal velocity and temperature perturbation spectra have very similar shapes for midfrequency GWs.

Figure 4a shows the 1-D horizontal velocity, vertical velocity, and temperature spectra that result when summing the 2-D spectra in Figure 3 over Δm. The spectra peak at $\lambda_H \sim 1,900$, 1,200, and 1,700 km, respectively. Figure 4b shows the same 1-D spectra, except summed over Δk and Δl. The spectra peak at $|\lambda_z| \sim 20$, 38, and 28 km, respectively. Figure 4c shows the same 1-D spectra, except as a function of $\overline{\tau_{lr}} = 2\pi/\overline{\omega_{lr}}$. Here $\overline{\omega_{lr}}$ is calculated via weighting the spectral amplitudes by ω_{lr} and summing over Δm:

$$\overline{\omega_{lr}} = \frac{\Sigma_m \omega_{lr} |\widetilde{u'_H}|^2}{\Sigma_m |\widetilde{u'_H}|^2}, \qquad \overline{\omega_{lr}} = \frac{\Sigma_m \omega_{lr} |\widetilde{w'}|^2}{\Sigma_m |\widetilde{w'}|^2}, \qquad \overline{\omega_{lr}} = \frac{\Sigma_m \omega_{lr} |\widetilde{T'}/\bar{T}|^2}{\Sigma_m |\widetilde{T'}/\bar{T}|^2}. \tag{45}$$

The spectra peak at $\overline{\tau_{lr}} \sim 5.5$, 3, and 4.5 hr, respectively. It is important to note that the midfrequency range whereby the u'_H and T' spectra have similar shapes occurs for $\tau_{lr} < 4.5$ hr. For larger periods (i.e., for $\tau_{lr} > 4.5$ hr $= 0.35 \times 2\pi/f$), f cannot be neglected. Figure 4d shows the same 1-D spectra as in Figure 4c, except as a function of the intrinsic horizontal phase speed $\overline{c_{lH}}$. Here $\overline{c_{lH}}$ is calculated via weighting the spectral amplitudes by c_{lH} and summing over Δk and Δl:

$$\overline{c_{lH}} = \frac{\Sigma_{k,l} c_{lH} |\widetilde{u'_H}|^2}{\Sigma_{k,l} |\widetilde{u'_H}|^2}, \qquad \overline{c_{lH}} = \frac{\Sigma_{k,l} c_{lH} |\widetilde{w'}|^2}{\Sigma_{k,l} |\widetilde{w'}|^2}, \qquad \overline{c_{lH}} = \frac{\Sigma_{k,l} c_{lH} |\widetilde{T'}/\bar{T}|^2}{\Sigma_{k,l} |\widetilde{T'}/\bar{T}|^2}. \tag{46}$$

The spectra peak at $\overline{c_{lH}} \sim 80$, 120, and 90 m/s, respectively.

Figure 5 shows the corresponding 1-D spectra for secondary GWs having azimuths of 10–30°. These spectra peak at larger λ_H and τ_{lr} and smaller $|\lambda_z|$ than the GWs with azimuths of 80–100°. Additionally, the vertical velocity amplitudes are smaller.

Figure 6 shows the 1-D spectra from Figure 4. We overlay lognormal functions of the form

$$A \exp\left(-\frac{\left[\log(\lambda) - \mu\right]^2}{2a^2}\right), \tag{47}$$

where λ is either λ_H or $|\lambda_z|$, A is the amplitude, μ is the peak value, and a is the width of the distribution. The values of A, μ, and a are given in the caption of Figure 6. The secondary GW spectra follow the lognormal

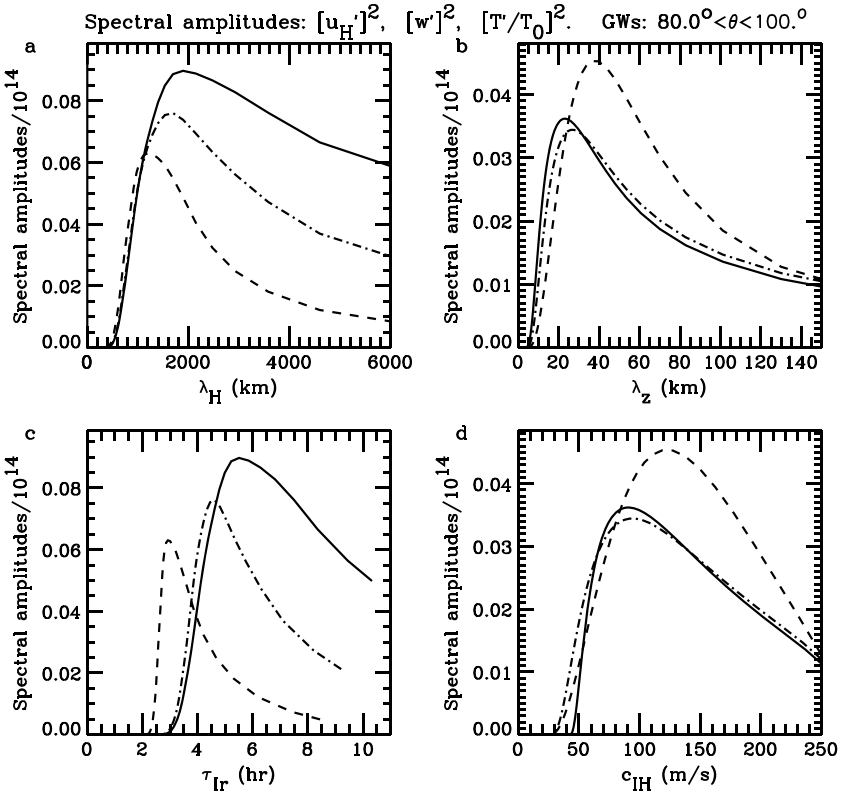

Figure 4. The 1-D spectra for the compressible solutions shown in Figure 3 for the secondary gravity waves (GWs) having azimuths of 80–100°. Solid, dashed, and dash-dotted lines show $\Sigma|\widetilde{u_H'}|^2\Delta k\Delta l\Delta m$, $\Sigma 3,000|\widetilde{w'}|^2\Delta k\Delta l\Delta m$, and $\Sigma 3\times10^5|\widetilde{T'}/\bar{T}|^2\Delta k\Delta l\Delta m$, respectively. These amplitudes are shown as functions of (a) λ_H, (b) $|\lambda_z|$, (c) τ_{Ir}, and (d) c_{IH}.

distributions reasonably well. In other words, the secondary GW wave number, period, and horizontal phase speed spectra created by body forces are strongly asymmetric about the peak values, with relatively large power (compared with a Gaussian distribution) at horizontal/vertical wavelengths, periods, and horizontal phase speeds that are much larger than the peak values.

Figure 7 shows the time evolution of the corresponding temperature perturbations at $y = 177$ km as a function of x and z. We "scale" $T'/\bar{T}$ by $\sqrt{\bar{\rho}}$ because a conservative upward or downward propagating GW in a constant wind and temperature has a constant density-scaled amplitude with height, $\sqrt{\bar{\rho}}T' \simeq$ constant; this scaling thus enables us to easily see the secondary GWs below and above the force equally. The secondary GWs radiate upward/downward and eastward/westward from the body force. These GWs are asymmetric in x about the force center; for example, at $z = 30$ km and $t = 8$ hr, T' at $x = -1,000$ km is opposite from its value at $x = 1,000$ km. The higher-frequency GWs (i.e., with steeper slopes and ray paths closer to the vertical) have larger vertical group velocities and therefore propagate more rapidly away from the force. The lower-frequency GWs (i.e., with shallower slopes and ray paths closer to the horizontal) have smaller vertical group velocities and therefore propagate more slowly away from the force. A small mean temperature response is left after the secondary GWs radiate away (i.e., at $x = -400$ to 400 km and $z = 40$–50 km in Figure 7d). This mean response is symmetric in x. In the region of the force, the asymmetric secondary GWs add and subtract from the symmetric mean response, thereby creating an asymmetric temperature structure at $t \leq 12$ hr.

Figure 8a shows the temperature perturbations from Figure 7a at $z = 59.7$ km and $t = 4$ hr. Figures 8b–8d show the associated wind perturbations. No GWs propagate perpendicular to the force direction (i.e., no GWs propagate solely in the y direction here). Importantly, T', u' and w' form arc-like partial concentric ring "headlights" in and against the direction of the force over subtended angles of ~60°, with maximum amplitudes at $y = 0$. The maximum amplitudes are $T' \sim 0.05\bar{T}/100 \simeq 0.1$ K and $u' \simeq 0.3$ m/s for this weak body force.

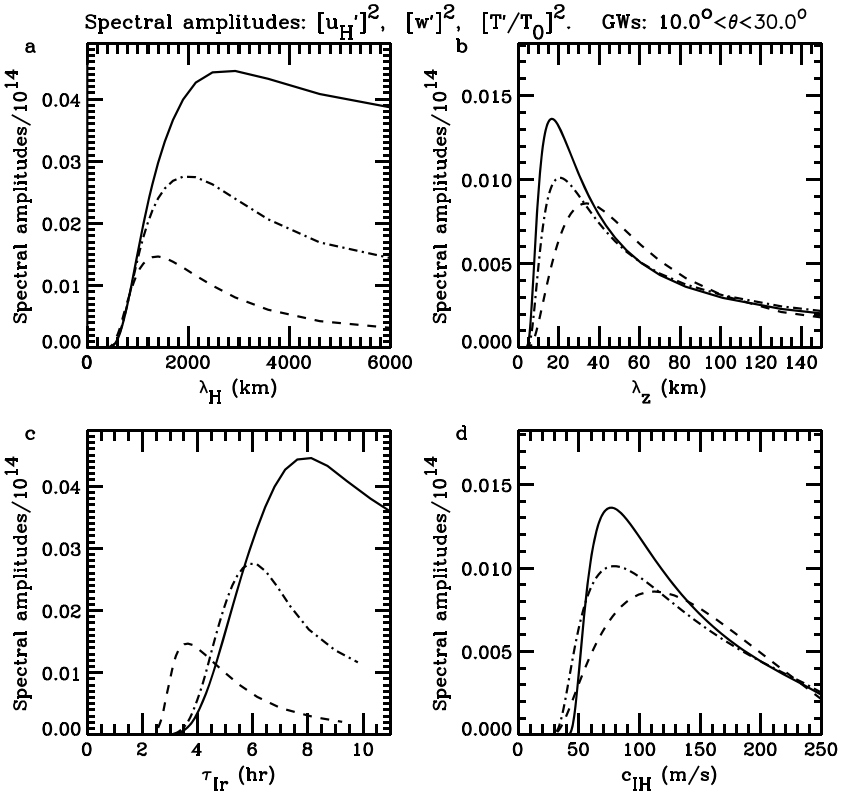

Figure 5. Same as Figure 4 but for the secondary gravity waves (GWs) propagating at azimuths of 10–30°.

Additionally, we see that λ_H increases with radius $\mathcal{R}$ from the body force center at $x = y = 0$ in Figure 8. We now show why this occurs. The GWs with larger $\mathcal{R}$ have larger intrinsic periods (Vadas et al., 2009):

$$\tau_{Ir} = \tau_B / \cos\vartheta, \tag{48}$$

where ϑ is the angle of the GW propagation direction from the zenith. Regardless of τ_{Ir}, the GWs that arrive at the same altitude z at the same time t must have the same vertical phase velocity:

$$c_z = \omega_{Ir}/m = \lambda_z/\tau_{Ir}. \tag{49}$$

Therefore, $|\lambda_z|$ is also larger for GWs at larger $\mathcal{R}$ at the same z and t, since

$$|\lambda_z| = |c_z|\tau_{Ir}. \tag{50}$$

The midfrequency GW dispersion relation for $|\lambda_z| << 4\pi\mathcal{H}$ is

$$\lambda_H \simeq |\lambda_z|\tau_{Ir}/\tau_B \tag{51}$$

from equation (32) with $m^2 >> k_H^2$ and $\tau_{Ir} < 4.5$ hr. Using equations (48) and (50), equation (51) becomes

$$\lambda_H \simeq \frac{|c_z|\tau_{Ir}^2}{\tau_B} \simeq \frac{|c_z|\tau_B}{\cos^2\vartheta} \simeq |c_z|\tau_B\left[\left(\frac{\mathcal{R}}{\Delta z}\right)^2 + 1\right], \tag{52}$$

where Δz is the distance from the force center to the altitude of interest. Therefore, λ_H increases as the radius squared when $\mathcal{R} > \Delta z$.

Figure 9 shows the mean wind, $\overline{u'}$ and $\overline{v'}$, created by this zonal body force. These horizontal mean wind responses are obtained by taking the temporal mean of the perturbation solutions in equations (14) and (15);

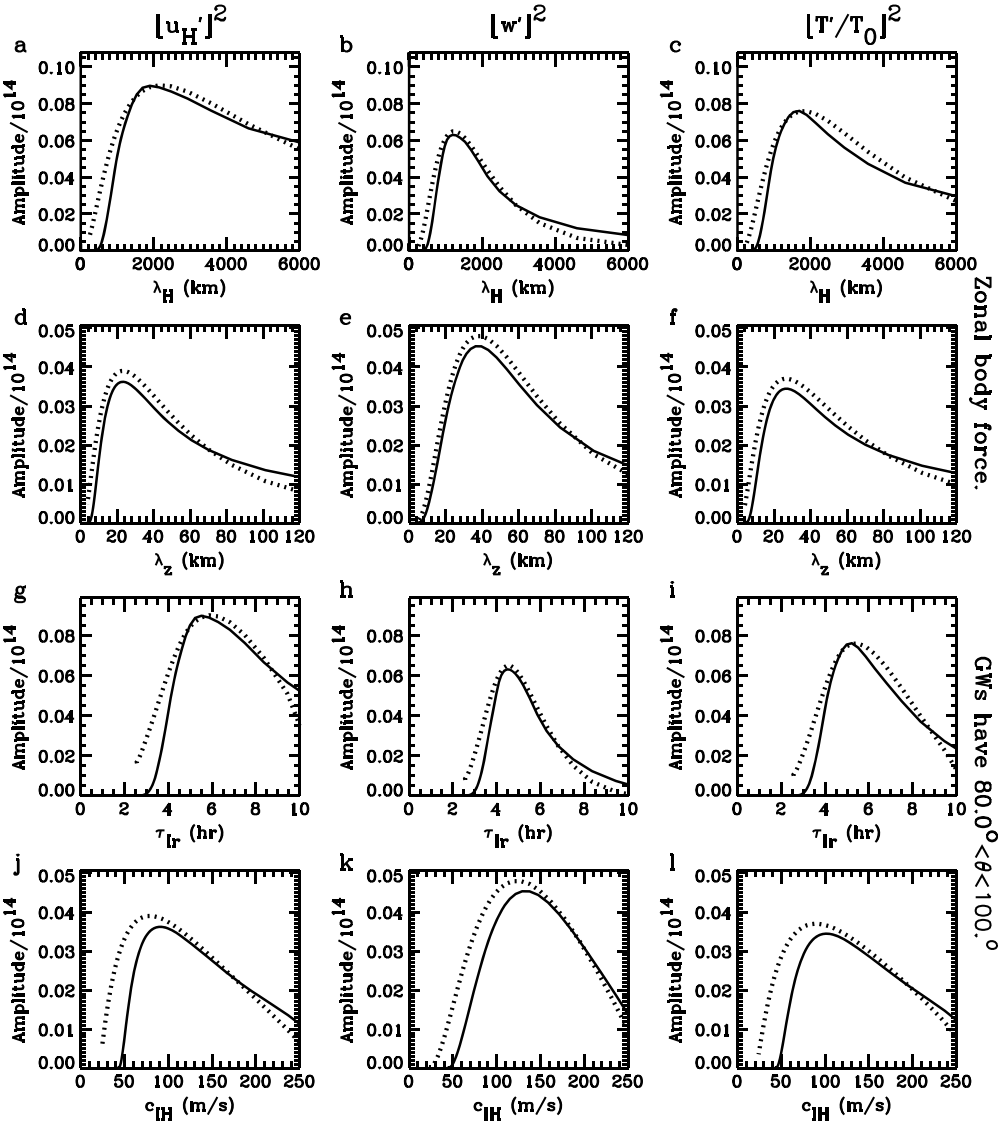

Figure 6. The 1-D spectra shown in Figure 4 (solid lines). We show (a) $\Sigma_m|\widetilde{u'_H}|^2\Delta k\Delta l\Delta m$, (b) $\Sigma_m 3,000|\widetilde{w'}|^2\Delta k\Delta l\Delta m$, (c) $\Sigma_m 3\times10^5|\widetilde{T'}/\bar{T}|^2\Delta k\Delta l\Delta m$ as functions of λ_H. (d–f) Same as row 1, but as functions of $|\lambda_z|$, and summed over Δk and Δl. (g–i and j–l) Same as (a)–(c) and (d)–(f) but as functions of $\overline{\tau_{lr}}$ and $\overline{c_{lH}}$, respectively (see equations (45) and (46)). Dotted lines show the lognormal distributions given by equation (47) with $A = 0.09$, $\mu = 7.7$ and $a = 1.0$ km (a and g); $A = 0.065$, $\mu = 7.12$ and $a = 0.62$ km (b and h); $A = 0.076$, $\mu = 7.5$ and $a = 0.82$ km (c and i); $A = 0.039$, $\mu = 3.14$ and $a = 0.92$ km (d and j); $A = 0.048$, $\mu = 3.64$ and $a = 0.69$ km (e and k); and $A = 0.037$, $\mu = 3.28$ and $a = 0.92$ km (f and l).

we denote these mean responses via the use of overlines on the primed perturbation variables in equation (8). A horizontal flow, $\overline{u'_H} = \sqrt{\overline{u'}^2 + \overline{v'}^2}$, containing two counterrotating cells is created in the region of the body force (Figure 9c). Figure 10 shows the total (GW plus mean responses) horizontal velocity induced by this body force at $z = 47.3$, 50.0, and 51.7 km. Close to the altitude of the force (i.e., at $z = 47.3$ km), the velocity looks similar to the mean flow (i.e., Figure 9c). At higher altitudes, the response is dominated by secondary GWs. This makes sense, because Figures 9a and 9b shows that the mean wind response extends only from $z = 42$–48 km. The secondary GWs appear to radiate outward in time, although the GWs at larger radii are actually different GWs having larger τ_{lr} and λ_H, as mentioned previously.

We determine the so-called "characteristic period" of the body force, τ_c, by assuming that the dominant GW excited by this force (if impulsive) would have $\lambda_H \sim 2\mathcal{D}_H$ and $|\lambda_z| \simeq 2\mathcal{D}_z$, where $\mathcal{D}_H = \mathcal{D}_x = \mathcal{D}_y$. We plug

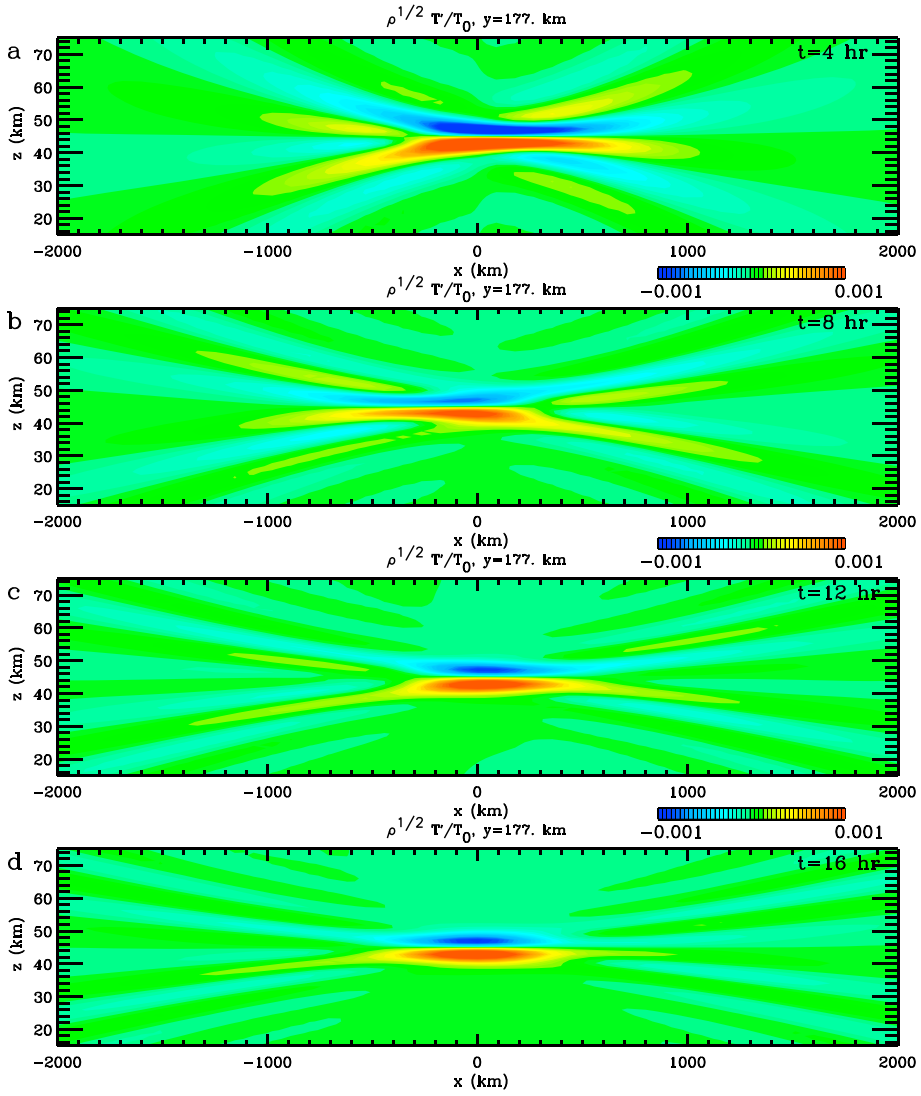

Figure 7. $\sqrt{\bar{\rho}}\,T'/\bar{T}$ (in $\sqrt{g/m^3}$) for the secondary gravity waves plus mean temperature perturbations created by the zonal body force with $\chi = 2$ hr at $y = 177$ km. (a) $t = 4$ hr. (b) $t = 8$ hr. (c) $t = 12$ hr. (d) $t = 16$ hr.

these wavelengths into the GW dispersion relation given by equation (32), similar to Vadas and Fritts (2001). τ_c is then the period of this assumed dominant GW. Since $\mathcal{D}_z << 2\pi\mathcal{H}$ and $\mathcal{D}_H >> \mathcal{D}_z$, we obtain

$$\tau_c \simeq \frac{2\pi \mathcal{D}_z^{-1}}{\sqrt{2\mathcal{D}_H^{-2}N_B^2 + \mathcal{D}_z^{-2}f^2}} \simeq \frac{\mathcal{D}_H}{\sqrt{2\mathcal{D}_z^2/\tau_B^2 + \mathcal{D}_H^2 f^2/(4\pi^2)}}. \quad (53)$$

For this force, $\tau_c \simeq 5.5$ hr. Because the force duration, $\chi = 2$ hr, satisfies $\chi \ll \tau_c$, the secondary GW spectra shown in the preceding figures are essentially the same as the secondary GW spectra created by an impulsive force with the same spatial dimensions (Vadas & Fritts, 2001).

We now calculate the compressible solution for the same zonal body force used to produce the spectra shown in Figure 4, but for a longer duration of $\chi = 6$ hr. Figure 11 shows the 1-D secondary GW spectra. The spectral peaks shift to larger λ_H and τ_{Ir} and smaller $|\lambda_z|$ and c_{IH}. For $|\widetilde{u'_H}|^2$, $|\widetilde{w'}|^2$, and $|\widetilde{T'}/\bar{T}|^2$, the spectral peaks occur at $\lambda_H \sim 3,000$, 1,600, and 1,900 km, $|\lambda_z| \sim 15$, 17, and 16 km, $\overline{\tau_{Ir}} \sim 8.5$, 6, and 7 hr, and $\overline{c_{IH}} \sim 75$, 70, and 65 m/s, respectively. Additionally, the vertical flux of horizontal momentum spectrum peaks at $\lambda_H \simeq 1,500$–2,500 km and $|\lambda_z| \simeq 15$–25 km (not shown). The duration of this force, $\chi = 6$ hr, is slightly larger than its characteristic period $\tau_c \simeq 5.5$ hr, which has the effect of cutting-off the highest-frequency secondary GWs with $\tau_{Ir} < \chi$ (Vadas & Fritts, 2001). This cut-off effect is seen in Figure 11b; the lack of high-frequency GWs causes all three

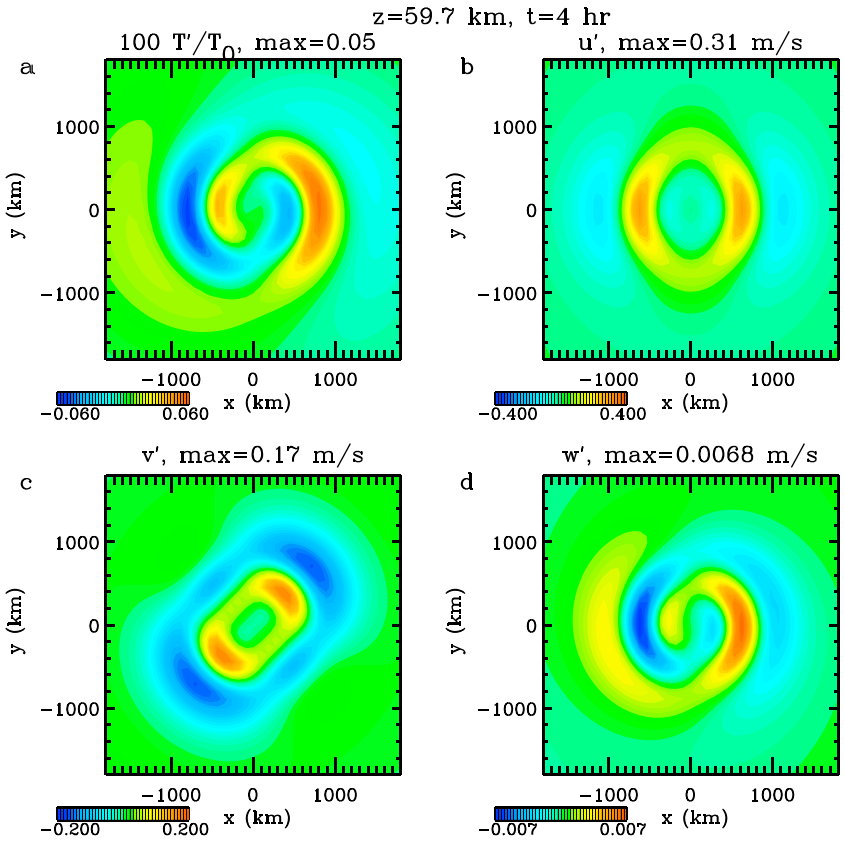

Figure 8. Perturbations created by the zonal body force with $\chi = 2$ hr at $t = 4$ hr and $z = 59.7$ km. (a) $100T'/\bar{T}$ (b) u'. (c) v'. (d) w'.

spectra to peak at similar $|\lambda_z|$ (as compared to Figure 4b). It can also be seen in Figure 11c, since there are few GWs with $\tau_{lr} < 6$ hr as compared to Figure 4c. Figure 12 shows $\sqrt{\bar{\rho}}\,T'/\bar{T}$ at $y = 177$ km. The lack of high-frequency GWs due to this cut-off effect as compared to Figure 7 is apparent at $t = 4$ and 8 hr. Although the secondary GW spectra differ, the mean response (associated with the counterrotating cells in the force region in Figure 9) is identical for both force durations (not shown). At $t = 4$ hr, there appears to be a dipole response centered at $x \sim -125$ km. This peculiar structure occurs because of the addition of the secondary GWs and mean response, which are asymmetric and symmetric in x, respectively, as discussed previously. A different time would yield a different structure. After the secondary GWs radiate out of the force region, the symmetric mean response is easily seen in the force region in Figure 12d.

We now determine what a horizontally displaced, vertically viewing observer (such as a lidar) would see in z-t plots for this idealized background (i.e., isothermal and constant wind). Figure 13 shows the scaled temperature perturbations for the zonal body force with $\chi = 2$ hr as a function of t and z at various locations in front of, behind, and to the side of the force. Because the GW phase lines move downward (upward) in time for an upward (downward) propagating GW, the secondary GW phase lines create coherent fishbone or ">" structures at all locations, with the knee of the structures, z_{knee}, occurring at the altitude of the body force center (i.e., at $z_{\text{knee}} = z_0$). Note that the lines are asymmetric in z about z_{knee}, which means that negative and positive phase lines converge at $z = z_{\text{knee}}$. At a given time at a fixed x, y location, 1) the GWs below and above z_{knee} propagate in the same direction away from the body force, and 2) τ_{lr}, $|\lambda_z|$, and the density-scaled GW amplitudes (i.e., $\sqrt{\bar{\rho}}$ times the GW amplitude) are the same below and above the knee.

The radius of this body force is 400 km at $z = z_0$. Figure 13a shows that when the observer is within the force region, there are only a few plus/minus GW phase lines within the fishbone structure. However, when the observer's location is 2 times the force radius (i.e., Figure 13b), there are ~5 plus/minus GW phase lines within the structure. When the observer's location is 5.7 times the force radius (i.e., Figure 13d), the GW phase lines have very small amplitudes close to z_{knee}, resulting in the appearance that the phase lines do not reach z_{knee}.

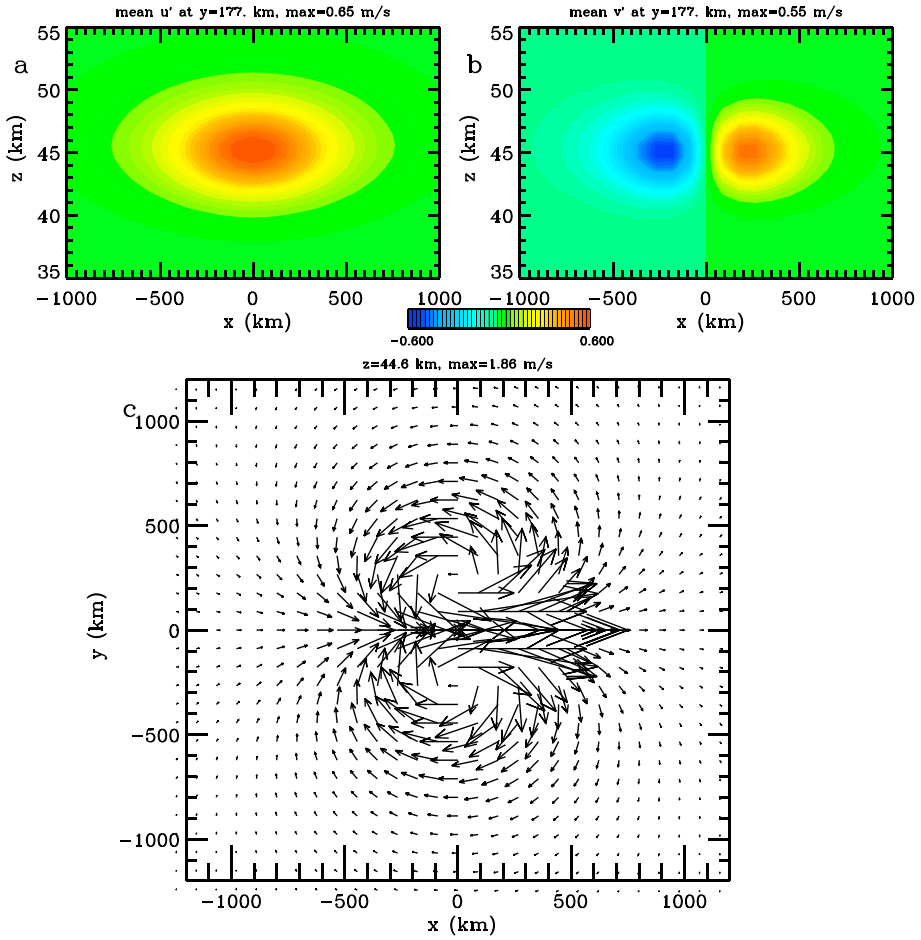

Figure 9. The mean zonal velocity, $\overline{u'}$, and the mean meridional velocity, $\overline{v'}$, induced by the same zonal body force as in Figure 7. (a) $\overline{u'}$ at $y = 177$ km. The maximum value is 0.65 m/s. (b) $\overline{v'}$ at $y = 177$ km. The maximum value is 0.55 m/s. (c) The mean horizontal velocity, $\overline{u'_H}$ at $z = 44.6$ km showing the counterrotating cells. The arrows show the direction, and the lengths are proportional to the magnitude. The maximum amplitude is 1.86 m/s.

Figure 14 shows the same result as Figure 13 but for the zonal body force with duration $\chi = 6$ hr. This structure has a somewhat smaller vertical extent because of the lack of the highest-frequency secondary GWs but is otherwise similar to Figure 13.

The result that τ_{lr}, $|\lambda_z|$ and the density-scaled GW amplitudes are exactly the same at any given time below and above z_{knee} in Figures 13 and 14 occurs because the background temperature and wind are assumed constant with altitude and time. Indeed, a wind shear or change in N_B would significantly change the appearance of this fishbone structure. If $|\lambda_z| < 2\pi\mathcal{H}$, the dispersion relation for a midfrequency or low-frequency GW (i.e., $m^2 \gg {k_H}^2$) is

$$\omega_{lr}^2 \simeq f^2 + {k_H}^2 {N_B}^2/m^2 \tag{54}$$

from equation (32). This can be rewritten as

$$\lambda_z \simeq \pm \frac{\lambda_H \sqrt{(\omega_r - k_H U_H)^2 - f^2}}{N_B}, \tag{55}$$

where we have used equation (2), which can be rewritten as

$$\tau_{lr} = \frac{1}{1/\tau_r - U_H/\lambda_H}. \tag{56}$$

Equation (55) shows the well-known result that $|\lambda_z|$ increases if a GW increasingly propagates against the wind (i.e., $\omega_r - k_H U_H$ increases along its ray path) and decreases if a GW increasingly propagates with the wind

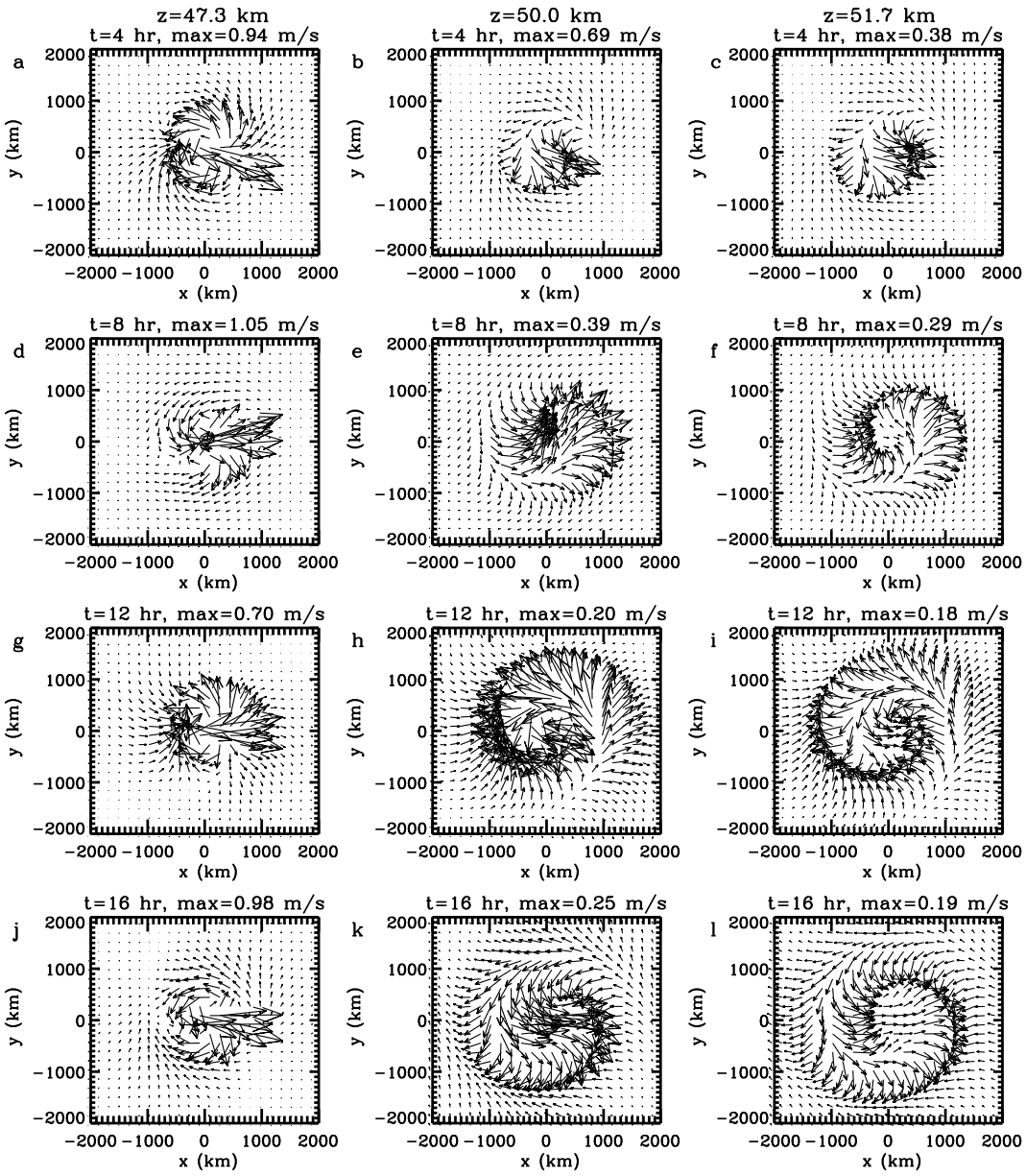

Figure 10. The total (gravity wave plus mean responses) horizontal velocity induced by the same zonal body force as in Figure 7. (a–c) The horizontal velocity at $t = 4$ hr at $z = 47.3$, 50.0, and 51.7 km, respectively. The arrows show the direction, and the lengths are proportional to the magnitude. (d–f, g–i, and j–l) show the same as the first row but for $t = 8$, 12, and 16 hr, respectively. The maximum amplitude in each panel is labeled.

(i.e., $\omega_r - k_H U_H$ decreases along its ray path). If $|\lambda_z|$ decreases significantly, then the GW is susceptible to dissipative processes such as wave breaking, which decreases a GW's amplitude.

Additionally, a GW is eliminated if it reaches a critical level whereby $\omega_{lr} = 0$. From equation (2), this occurs at $\omega_r = k_H U_H$ or

$$U_H = \frac{\lambda_H}{\tau_r}. \tag{57}$$

Importantly, as long as a GW avoids critical level filtering or breaking, τ_r is constant as a GW propagates through a *stationary* (in time) vertical or horizontal wind shear, even though τ_{lr} changes via equation (56). Therefore, because the upward and downward propagating secondary GWs with the same **k** have the same initial τ_r (because they have the same initial τ_{lr}), the secondary GWs below and above z_{knee} have the same τ_r

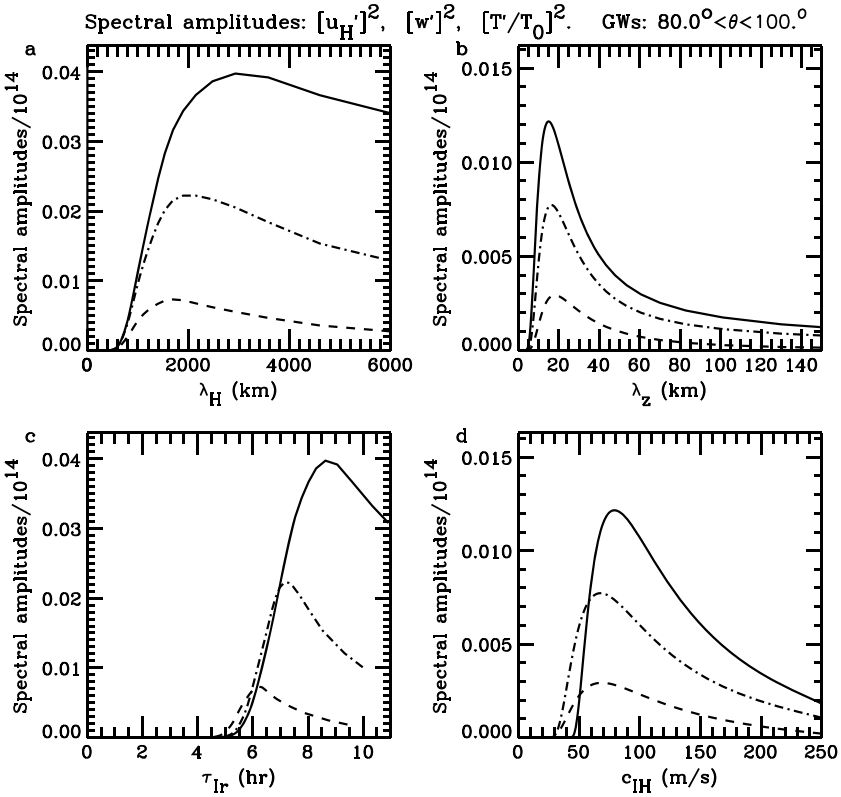

Figure 11. Same as Figure 4 but for the zonal body force with $\chi = 6$ hr. GWs = gravity waves.

even if they propagate through different vertical or horizontal wind shears, as long as those shears are stationary. This is not true for τ_{Ir}. The exception is if the background changes in time: $\partial\bar{U}/\partial t \neq 0$, $\partial\bar{V}/\partial t \neq 0$, $\partial\bar{\rho}/\partial t \neq 0$, or $\partial\bar{T}/\partial t \neq 0$. In these cases, ω_r changes in time (Eckermann & Marks, 1996; Senf & Achatz, 2011). The equation describing this change is (Lighthill, 1978)

$$\frac{d\omega_r}{dt} = k\frac{\partial\bar{U}}{\partial t} + l\frac{\partial\bar{V}}{\partial t} + \frac{\partial\omega_{Ir}}{\partial t}, \tag{58}$$

where dt is integrated along the ray path and $\partial/\partial t$ is computed for fixed **k** and **x**. Note that $\partial\omega_{Ir}/\partial t$ contains terms proportional to $\partial\mathcal{H}/\partial t$ and $\partial N_B/\partial t$ through the dispersion relation. The first two terms on the right-hand side of equation (58) can be important for MWs when the eastward wind accelerates in the lower stratosphere (Vadas & Becker, 2018). Therefore, when examining GWs in a fishbone structure whereby the background wind shear is relatively stationary, it is best to compare τ_r below and above z_{knee} (rather than τ_{Ir}) in order to help determine if the GWs are secondary GWs.

Critical level filtering of some of the GWs in the secondary GW spectrum via equation (57) can create a significant asymmetry in the scaled amplitudes of the fishbone structure below and above z_{knee}. This is because these secondary are part of a broad spectrum of midfrequency and low-frequency GWs with a wide range of c_{IH} (see Figure 4d). Those that have large (small) c_{IH} are less (more) affected by the background wind shear. Thus, only part of a secondary GW spectrum is affected by a wind shear. If a shear is large enough, the fishbone structure would be altered whereby one-half of the GWs (either below or above z_{knee}) would have smaller density-scaled amplitudes than those in the other half due to wave attenuation from small $|\lambda_z|$.

Finally, a single lidar cannot measure a GW's propagation direction. However, it is possible in some cases to infer the propagation direction of the secondary GWs in a fishbone structure to within 180° if there is an asymmetry in the amplitude of the structure (e.g., if the scaled amplitudes are smaller below than above z_{knee}) and the background wind is known. We explore this concept further in section 4 when we analyze several fishbone structures in lidar data.

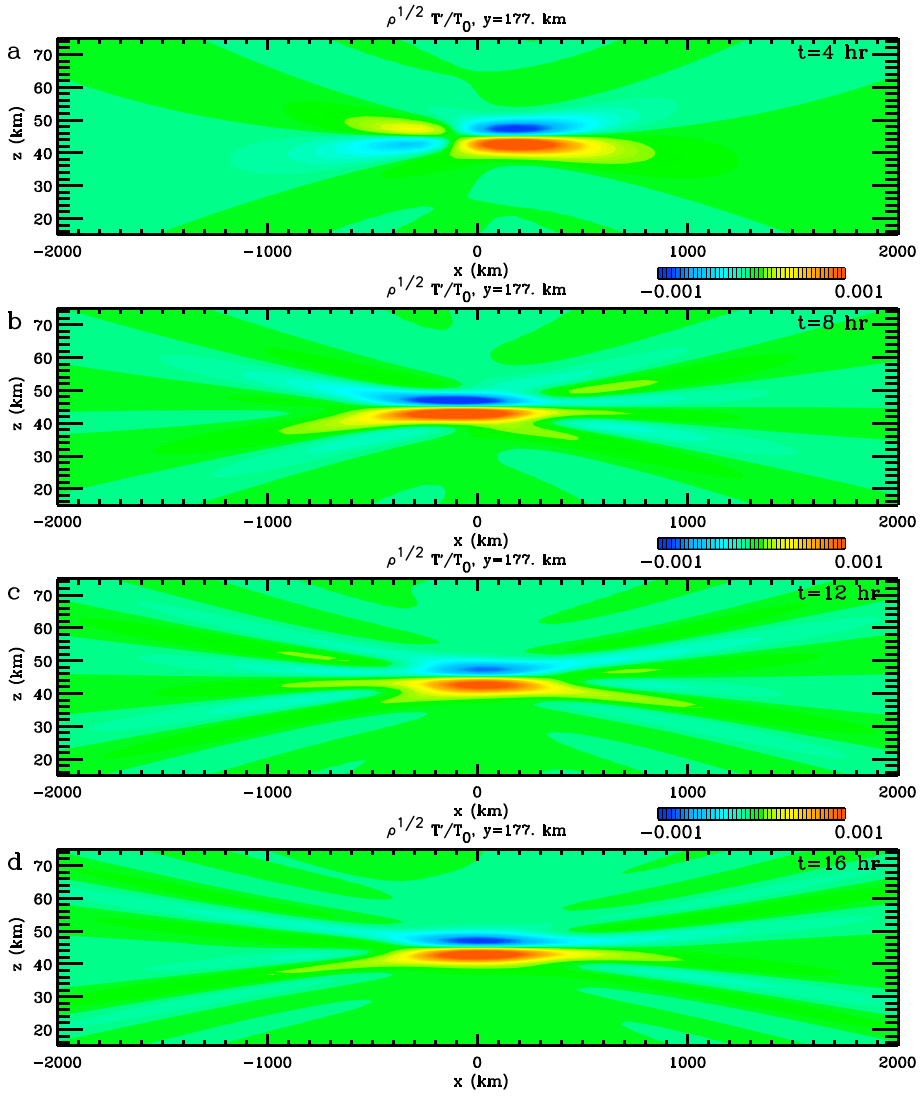

Figure 12. Same as Figure 7 but for the zonal body force with $\chi = 6$ hr.

4. Secondary GWs Within Fishbone Structures in McMurdo Lidar Data

In this section we analyze two cases where fishbone structures are seen in temperature data measured by an Fe Boltzmann temperature lidar at Arrival Heights (166.69°E, 77.84°S) near McMurdo, Antarctica (Chu et al., 2002; Chu, Huang, et al., 2011; Chu, Yu, et al., 2011). For the cases shown here, we derive the temperatures from the pure Rayleigh scattering region at $z \sim 30–70$ km using the Rayleigh integration technique (Alexander et al., 2011; Chu et al., 2009; Fong et al., 2014; Kaifler et al., 2015; Klekociuk et al., 2003; Lu et al., 2015, 2017; Wilson et al., 1991; Yamashita et al., 2009; Zhao et al., 2017). All lidar data used here have 1-hr temporal resolution and 1-km vertical resolution.

The two cases we analyze here show clear evidence of fishbone structures in *z-t* plots of the density-scaled relative temperature perturbations (i.e., $\sqrt{\bar{\rho}}T'/\bar{T}$). That is, GWs with downward phase progression are seen above a possible knee, and GWs with upward phase progression are seen below this knee, similar to Figures 13 and 14. These cases were chosen in large part because τ_r and $|\lambda_z|$ are similar below and above z_{knee}, which suggests that if a background wind shear is present, it is not too strong. If the background wind or N_B changes substantially along the GW ray paths, it would be necessary to perform body force modeling and ray tracing to determine how the structure would appear in a *z-t* plot. Such studies are beyond the scope of this paper.

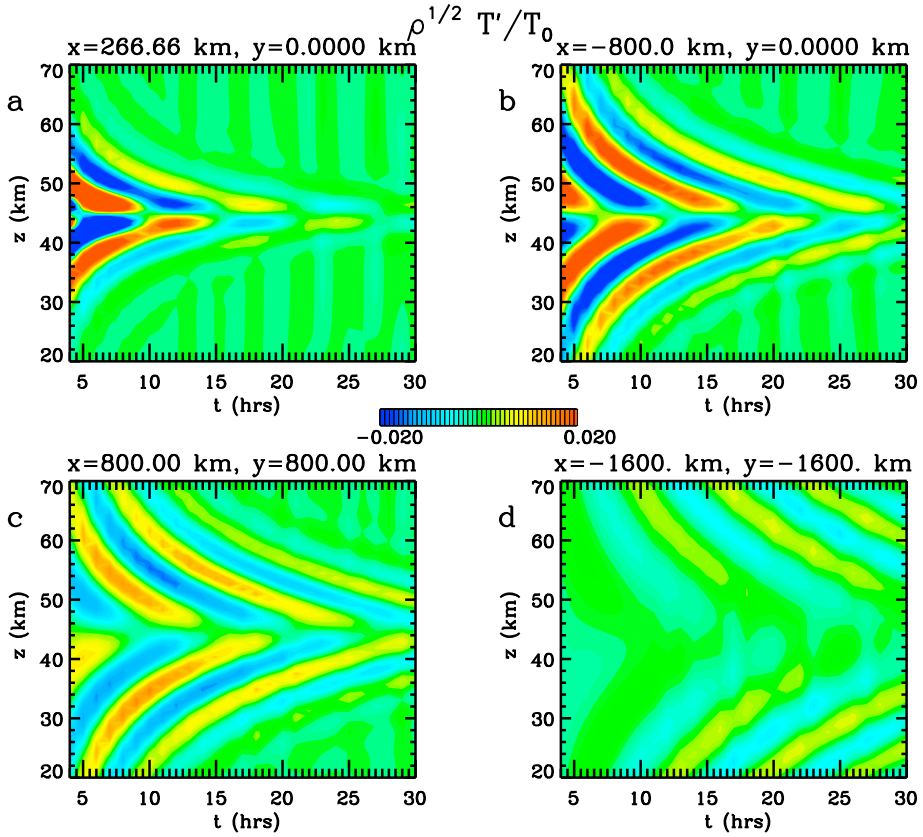

Figure 13. The scaled temperature perturbations, $\sqrt{\bar{\rho}}T'/\bar{T}$ (in $\sqrt{\mathrm{g/m^3}}$), for the same zonal body force with $\chi = 2$ hr as in Figure 7 at (a) $x = 267$ km and $y = 0$, (b) $x = -800$ km, and $y = 0$, (c) $x = 800$ km and $y = 800$ km, and (d) $x = -1,600$ km and $y = -1,600$ km.

Our analysis for each chosen case is as follows. We first *assume* that the GWs in the fishbone structure are secondary GWs. We also assume that downward (upward) phase progression corresponds to upward (downward) propagating GWs. Our analysis for each chosen case will validate these assumptions. In the following, we describe this analysis along with corresponding criteria in detail.

We first calculate the scaled GW amplitudes, $\sqrt{\bar{\rho}}T'/\bar{T}$, and remove all waves with $\tau_r > 11$ hr. We estimate the altitude of the knee for the structure, z_{knee}, by eye via requiring the following:

1. The structure is asymmetric in z about z_{knee}, that is, the cold and hot phase lines (from below and above) converge at z_{knee}. An incorrect estimate for z_{knee} (whereby the structure is symmetric in z) yields an incorrect vertical range for the calculated spectra below and above z_{knee}, which results in incorrectly determined (biased) GW parameters below and above z_{knee}.
   We then remove all upward (downward) propagating GWs below (above) z_{knee} to isolate the fishbone structure. We identify by eye the temporal and vertical extent for the structure. Then, we require that the following criteria are met:
2. If upward propagating (i.e., downward phase progression) GWs are present below z_{knee}, their amplitudes are partially or fully damped at least a few kilometers below z_{knee}. This allows for a possible excitation mechanism for the secondary GWs;that is, that the primary GWs dissipate and create a body force. However, the center of the body force would need to be horizontally displaced in order to see the secondary GWs.
3. If upward propagating GWs are present below z_{knee}, $|\lambda_z|$ does not become extremely large near z_{knee}. This rules out the possibility that the primary GWs reflect downward at z_{knee}, which could be mistaken for downward propagating secondary GWs.

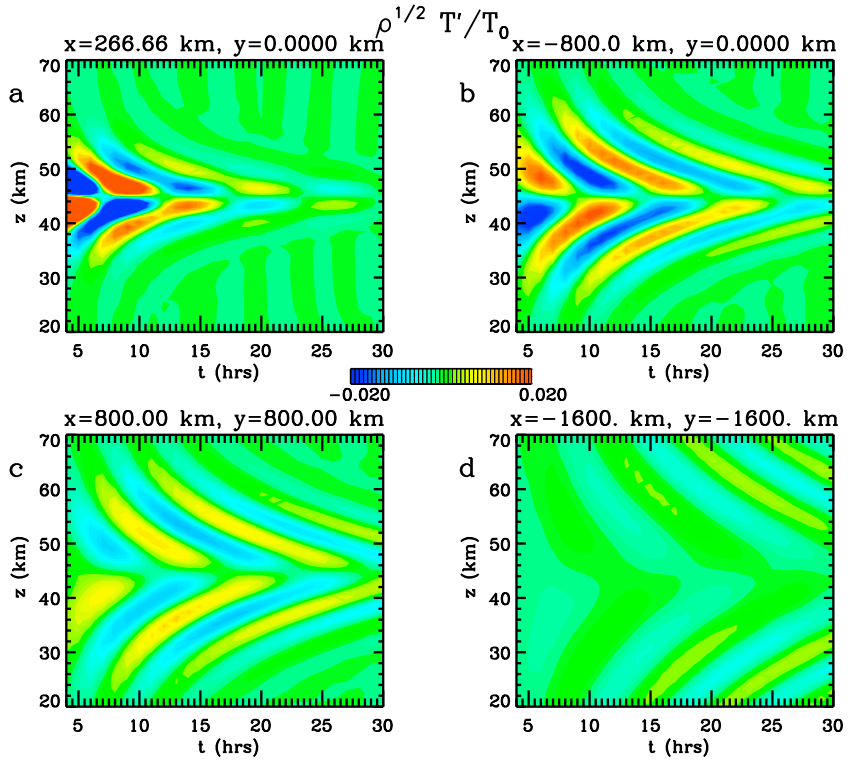

Figure 14. Same as Figure 13 but for the zonal body force with $\chi = 6$ hr.

4. If downward propagating GWs are present above z_{knee}, they only have small density-scaled amplitudes relative to the scaled amplitudes of the downward propagating GWs at $z < z_{knee}$. This helps eliminate overly complicated cases.

   We then calculate the spectra below and above z_{knee} separately for the secondary and removed GWs and determine the peak values of τ_r and λ_z. We require the following:
5. The peak values of $|\lambda_z|$ and τ_r for the removed GWs below z_{knee} are different than that for the secondary GWs above z_{knee}. This ensures that the upward propagating secondary GWs are not continuations of the upward propagating primary GWs.
6. The peak values of $|\lambda_z|$ and τ_r for the removed GWs above z_{knee} are different than that for the secondary GWs below z_{knee}. This ensures that the downward propagating secondary GWs are not continuations of the downward propagating GWs above z_{knee}.

   We then check the validity of our first assumption, that is, that the GWs in the fishbone structure are secondary GWs. Since secondary GWs in an unsheared, isothermal atmosphere have the same τ_r, $|\lambda_z|$ and scaled amplitudes below and above z_{knee} (see section 3), we require the following:
7. The parameters τ_r and $|\lambda_z|$ are similar below and above z_{knee}, and the scaled amplitudes are within a factor of 2–2.5 below and above z_{knee}. (Here we allow for a significant difference of the GW amplitudes because even small shears can dissipate a large portion of the secondary GW spectrum if it peaks at small to medium c_{IH}.)

   Finally, we check the validity of our last assumption, that is, that the GWs in the fishbone structure having upward (downward) phase progression are downward (upward) propagating GWs. We do this via requiring the following:
8. In the vicinity of z_{knee}, c_{IH} is greater than $|\bar{U}|$ and $|\bar{V}|$ (see explanation below). Note that this is an overly conservative estimate if the GW primarily propagates meridionally, because $|\bar{U}|$ is often much larger than $|\bar{V}|$. If the GW propagation direction is known, we would instead compare c_{IH} directly with U_H.

If criteria #1–8 are met, we then conclude that the fishbone structure is likely comprised of secondary GWs excited by a horizontally displaced body force at the altitude $z = z_{knee}$.

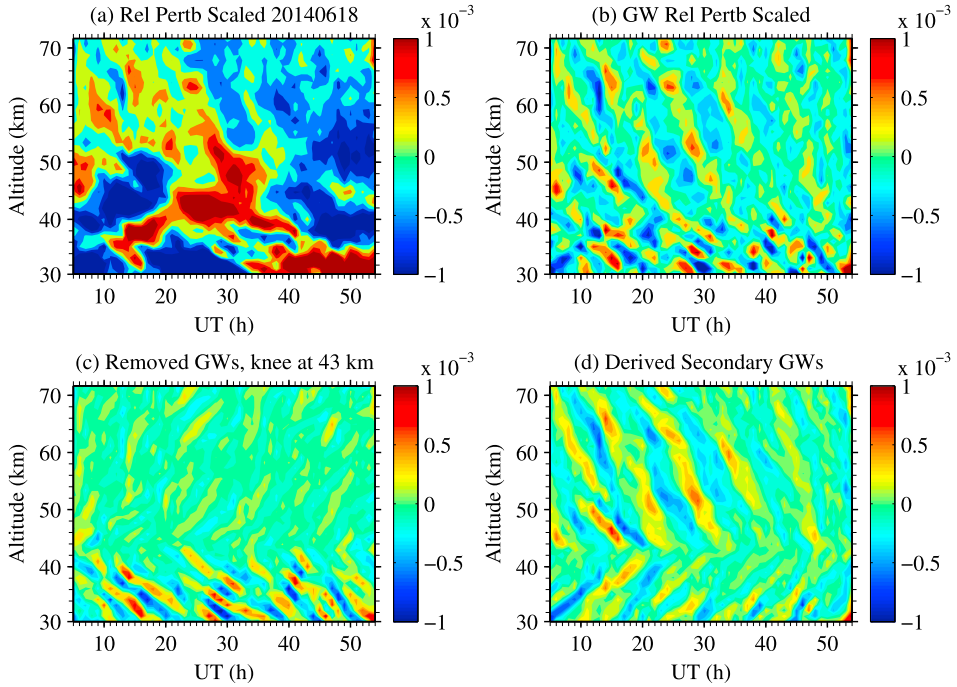

Figure 15. (a) Scaled temperature perturbations, $\sqrt{\bar{\rho}}T'/\bar{T}$, on 18 June 2014 using equation (59). (b) As in (a) but only retaining GWs with periods ≤ 11 hr. (c) Removed GWs from (b), obtained by selecting GWs with upward phase progression for $z > z_{knee}$ and downward phase progression for $z < z_{knee}$. Here $z_{knee} = 43$ km. (d) Derived secondary GWs, obtained by subtracting (c) from (b). Color bars are in units of $\sqrt{kg/m^3}$. GW = gravity wave.

4.1. Case 1: 18 June 2014

The first case we analyze is on 18 June 2014. Figure 15a shows the density-scaled temperature perturbations,

$$\sqrt{\bar{\rho}}\frac{T'}{\bar{T}} = \sqrt{\bar{\rho}}\frac{(T-\bar{T})}{\bar{T}}, \tag{59}$$

where $\bar{T}$ is the temperature averaged over the temporal range of the displayed data at each altitude. Additionally, $\bar{\rho}$ is the background density (in kg/m^3) taken from NRLMSISE-00 (Picone et al., 2002), averaged over the entire month (i.e., June 2014 here). (We do not use the Rayleigh lidar data to estimate $\bar{\rho}$ because it includes strong wave perturbations and the data are not evenly distributed in time.) Large-amplitude waves with ~1-day periods are seen; these are likely due to eastward propagating planetary waves with periods of 1–5 days (Lu et al., 2013, 2017). Figure 15b shows $\sqrt{\bar{\rho}}T'/\bar{T}$ after waves with $\tau_r > 11$ hr are removed via Fourier filtering using a sixth-order Butterworth filter. Constructive and destructive interference is seen for upward and downward propagating GWs at $z < 45$ km. For 5–55 UT, nearly all of the GWs at $z > 45$ km are upward propagating. Importantly, at 5–30 UT, GWs with upward phase progression are present at $z = 30$–42 km, and GWs with downward phase progression and having similar τ_r and $|\lambda_z|$ are present at $z = 45$–60 km, thus suggesting that these GWs are part of a fishbone structure. From Figure 15b, we estimate (by eye) that $z_{knee} \simeq 43$ km following criterion #1.

We now investigate if these GWs are part of a fishbone structure with $z_{knee} = 43$ km. We apply a Fourier filter to each altitude range individually. For $z < z_{knee}$, we remove those GWs with downward phase progression, and for $z > z_{knee}$, we remove those GWs with upward phase progression. We show these removed GWs in Figure 15c. Relatively large-amplitude GWs with downward phase progression occur at $z < z_{knee}$. These GWs are likely upward propagating primary GWs from the troposphere or lower stratosphere (e.g., MWs or Inertia-GWs from regions of imbalance). Importantly, these GWs are severely damped by $z \simeq 35$–40 km, thereby satisfying criterion #2. Additionally, the phase lines do not become vertical near z_{knee}, thereby satisfying criterion #3. Additionally, only small-amplitude GWs with upward phase progression occur above z_{knee}, thereby satisfying criterion #4.

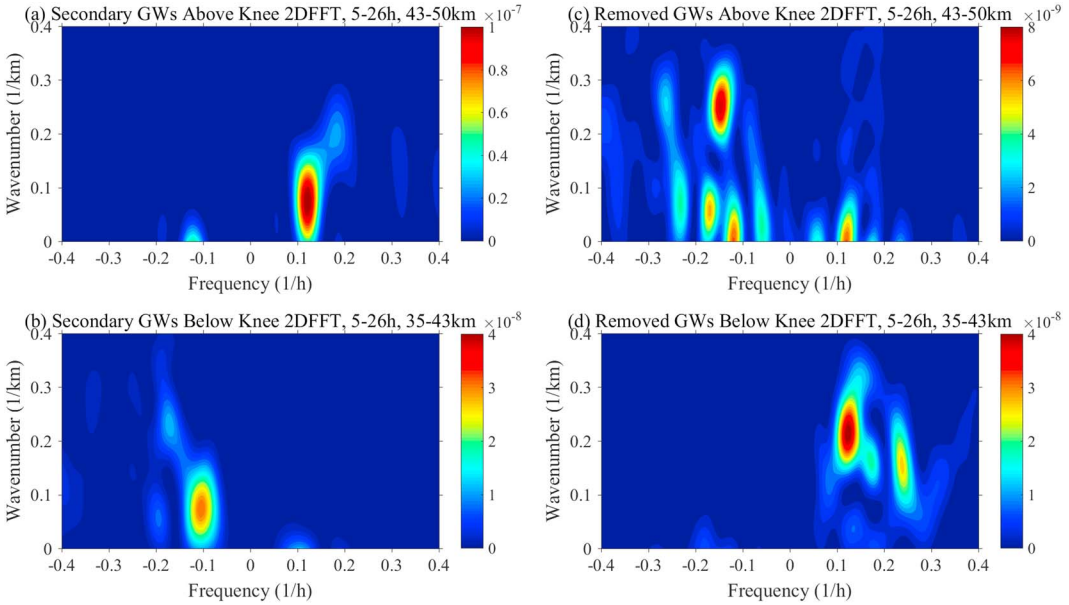

Figure 16. (a and b) Power spectral density of $\sqrt{\bar{\rho}}T'/\bar{T}$ for the derived secondary GWs from Figure 15d for 5–26 UT as a function of wave number and frequency: (a) above the knee using data for z = 43–50 km and (b) below the knee using data for z = 35–43 km. Negative (positive) frequency denotes upward (downward) phase progression. (c and d) Same as (a) and (b) but for the removed GWs in Figure 15c. GW = gravity wave; FFT = fast Fourier transform.

Figure 15d shows the derived secondary GWs, obtained by subtracting Figure 15c from Figure 15b. The fishbone structure is clearly visible for $z = 30 - 60$ km at 0–30 UT. Note that the scaled amplitudes are smaller below z_{knee} after 20 UT.

We now determine the parameters of the secondary and removed GWs. We define the extent of the fishbone structure to be $t = 5 - 26$ UT and $z = 35 - 50$ km. We take the 2-D fast Fourier transform (FFT) of $(\sqrt{\bar{\rho}}T'/\bar{T})$ for the secondary and removed GWs below and above z_{knee} separately, which we denote as $\widetilde{(\sqrt{\bar{\rho}}T'/\bar{T})}$. The widetilde "~" encompasses all factors within the parenthesis. Here we apply the 2-D FFT directly to the chosen time-altitude area, with no window. We calculate the power spectral density (PSD) of the derived secondary and removed GWs via computing $\widetilde{(\sqrt{\bar{\rho}}T'/\bar{T})}\widetilde{(\sqrt{\bar{\rho}}T'/\bar{T})}^{*}$, where "*" denotes the complex conjugate. The results are shown in Figure 16. A single dominant large peak occurs in each PSD. To calculate the peak parameters and their error bars of the secondary and removed GWs, we utilize a Monte Carlo procedure with 500 simulations. For each simulation, we reconstruct the temperature field over time and altitude. Each temperature value on the reconstructed temperature field is composed of the sum of the lidar observed temperature and a deviation. The deviation is simulated by a randomly generated Gaussian white noise, which is randomly drawn from a Gaussian distribution with a mean of 0 and a standard deviation equal to the lidar observed temperature uncertainty at this grid point. For this simulated temperature field, we then separate the secondary and removed GWs and calculate the PSDs below and above z_{knee} (as explained above). The peak parameters are then obtained by calculating the PSD weighted average for the 500 simulations. The error caused by the temperature uncertainty is obtained by calculating the PSD weighted standard deviation for the 500 iterations. The final error bar for each parameter includes this Monte Carlo temperature uncertainty error, the temporal or vertical binning resolution error, and the FFT resolution error via taking the square root of their squared sum.

The peak parameters of the secondary and removed GWs are given in Table 1. The secondary GW parameters above z_{knee} have $\tau_r = 8.26 \pm 0.52$ hr and $|\lambda_z| = 13.62 \pm 2.20$ km. In contrast, the removed GW parameters below z_{knee} have $\tau_r = 8.09 \pm 0.53$ hr and $|\lambda_z| = 4.67 \pm 0.52$ km. Because $|\lambda_z|$ for the removed GWs is much smaller than that for the secondary GWs, we conclude that the upward propagating secondary GWs at $z > z_{knee}$ are not continuations of the upward propagating removed GWs at $z < z_{knee}$. Thus, criterion #5 is satisfied. Additionally, the secondary GW parameters below z_{knee} have $\tau_r = 9.54 \pm 0.57$ hr and $|\lambda_z| = 13.55 \pm 1.22$ km. In contrast, the removed GW parameters above z_{knee} have $\tau_r = 6.82 \pm 0.53$ hr and $|\lambda_z| = 3.98 \pm 0.54$ km.

Table 1
Parameters of the GWs on 18 June 2014

	Below knee		Above knee	
GW type	τ_r (hr)	$\lvert\lambda_z\rvert$ (km)	τ_r (hr)	$\lvert\lambda_z\rvert$ (km)
Secondary GWs	9.54 ± 0.57	13.55 ± 1.22	8.26 ± 0.52	13.62 ± 2.20
Removed GWs	8.09 ± 0.53	4.67 ± 0.52	6.82 ± 0.53	3.98 ± 0.54

Note. GWs = gravity waves.

Because the $|\lambda_z|$s are again quite different, we conclude that the downward propagating secondary GWs at $z < z_{\text{knee}}$are not continuations of the downward propagating removed GWs at $z > z_{\text{knee}}$. Thus, criterion #6 is satisfied. Therefore, we have shown that the derived secondary GWs are not continuations of the removed GWs below and above z_{knee}. Importantly, τ_r and $|\lambda_z|$ for the secondary GW below and above z_{knee} are quite similar. From Figure 15d, the scaled secondary GW amplitudes below and above z_{knee} are (0.25–0.6) and (0.25–1.0) $\sqrt{\text{kg/m}^3}$, respectively. Although the variation in the scaled amplitudes is large below and above z_{knee}, they are within a factor of 2–2.5 of each other. Therefore, criterion #7 is satisfied.

We now check our assumption that upward (downward) phase progression corresponds to downward (upward) propagating secondary GWs. If an upward propagating GW is propagating against the background wind with $U_H < 0$ and $|U_H| > c_{IH}$ (e.g., the GW propagates against the background wind but is swept downstream in the same direction as the wind), then its phase lines are upward (not downward) in time in a $z - t$ plot (Dörnbrack et al., 2017; Fritts & Alexander, 2003). The opposite is true for a downward propagating GW. This can be seen by dividing equation (2) by k_H:

$$c_{IH} = c_H - U_H. \tag{60}$$

The condition for upward (downward) phase progression for upward (downward) propagating GWs is that $c_H < 0$. (Stationary MWs have $c_H = 0$.) Since by definition $k_H \geq 0$ and $c_{IH} \geq 0$ (because otherwise the GW would have already been attenuated at a critical level), then $c_H < 0$ if $U_H < 0$ and $|U_H| > c_{IH}$.

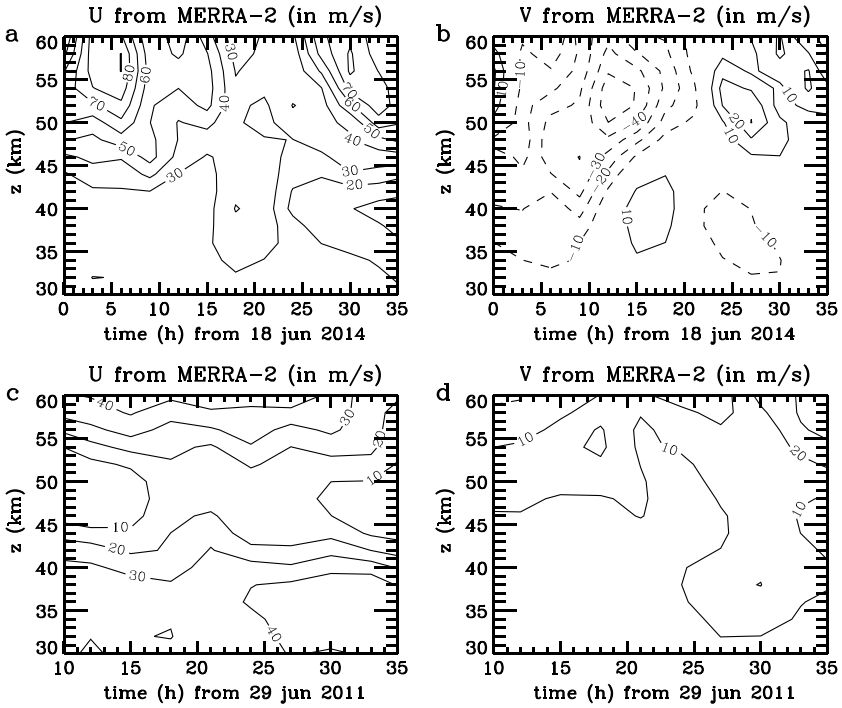

Figure 17. Background wind from Modern-Era Retrospective analysis for Research and Applications, version 2 (MERRA-2) at McMurdo. (a) $\bar{U}$ and (b) $\bar{V}$ on 18 June 2014. (c and d) Same as (a) and (b) but on 29 June 2011. Solid (dashed) lines show positive (negative) values.

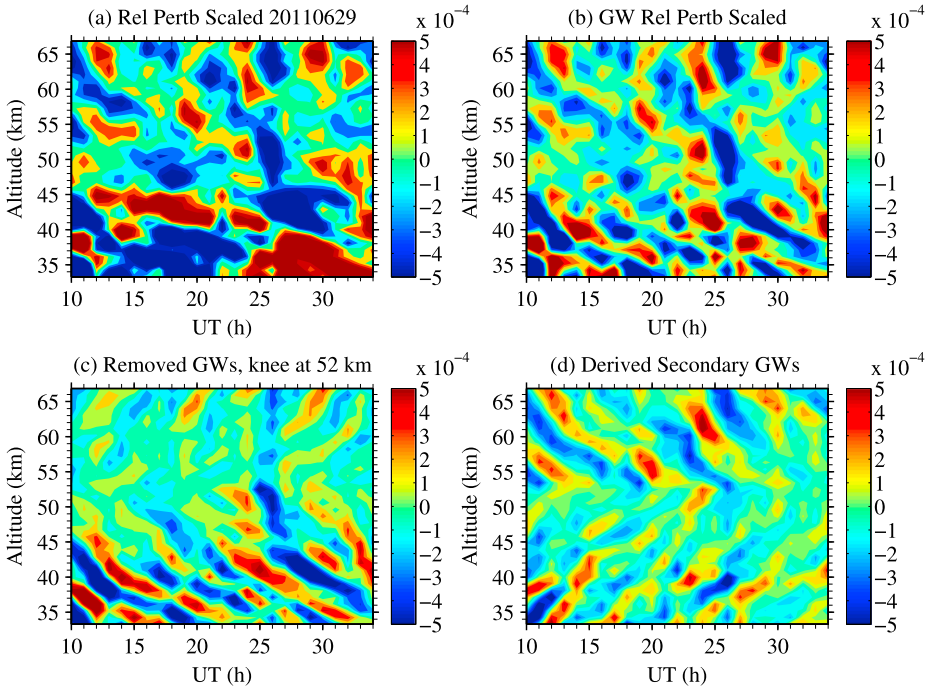

Figure 18. Same as Figure 15 but for 29 June 2011 with z_{knee} = 52 km. GW = gravity wave.

Such a phenomenon can occur if the background wind accelerates significantly, thereby sweeping an oppositely propagating GW downstream. For example, Vadas and Becker (2018) examined a westward quasi-stationary MW that propagated into an accelerating eastward wind. This caused its ground-based frequency ω_r to become negative because k remained negative. The result was that $c_H = \omega_r/k_H$ became negative, although the zonal phase speed became positive: $c_x = \omega_r/k > 0$. At and above the altitude where this acceleration occurred, the MW had upward phase progression. From equation (1), $U_H = k\bar{U}/k_H = sign(k)\bar{U} < 0$ in this case. This situation is analogous to a swimmer swimming upstream in a river. If the flow accelerates significantly, then the swimmer is swept downstream even though she continues swimming upstream relative to the flow.

Because wind observations are unavailable, we now apply this criterion by utilizing $\bar{U}$ and $\bar{V}$ from MERRA-2 (Modern-Era Retrospective analysis for Research and Applications, version 2). These winds are shown in Figures 17a and 17b at McMurdo. Above z_{knee}, the wind is southeastward with an amplitude of ~20–70 m/s within the structure extent. Below z_{knee}, the wind is southeastward at 5–12 UT and 20–26 UT and is northeastward at 12–20 UT with an amplitude of 10–40 m/s.

We now infer the secondary GW intrinsic horizontal phase speed from our observational analysis. From the midfrequency dispersion relation, a GW's intrinsic phase speed is

$$c_{IH} = \frac{\omega_{Ir}}{k_H} = N_B m = \frac{|\lambda_z|}{\tau_B}, \tag{61}$$

where $\tau_B = 2\pi/N_B$ is the buoyancy period. For the structure extent, $\tau_B \simeq 5.0$ min from MERRA-2. Using λ_z from Table 1, we infer $c_{IH} = 45$ m/s for the secondary GWs. We now compare c_{IH} with $\bar{U}$ and $\bar{V}$, similar to Kaifler et al. (2017). From Figures 17a and 17b, $c_{IH} > \sqrt{\bar{U}^2 + \bar{V}^2}$ is satisfied below z_{knee}. Therefore, the secondary GWs with upward phase progression below z_{knee} are downward propagating. The situation above z_{knee} is more complicated. The condition $c_{IH} > \sqrt{\bar{U}^2 + \bar{V}^2}$ is satisfied for all times at z = 43–50 km except at z = 46 − 50 km for 5–11 UT *if* the GWs have significant eastward propagation (i.e., $c_x > 0$). If these GWs propagate mainly meridionally, however, they would be upward propagating with downward phase progression at all altitudes and times. Because the secondary GWs are upward propagating at z = 43–46 km at 5–26 UT, and because the phase lines do not significantly change slope at and above z = 46 km in Figure 15d (as they would if they were propagating zonally and encountered the strong eastward wind shear in Figure 17a at 5–10 UT, which would

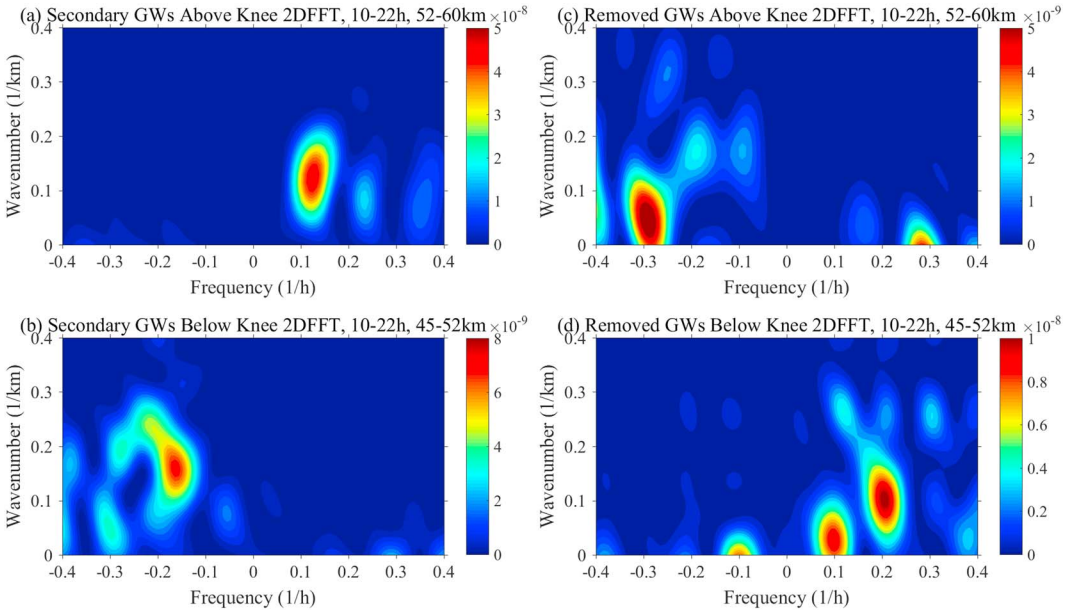

Figure 19. Same as Figure 16 but for 29 June 2011 at 10–22 UT using data for $z = 52–60$ km above the knee and for $z = 45–52$ km below the knee. $z_{knee} = 52$ km here. GW = gravity wave; FFT = fast Fourier transform.

have significantly changed $|\lambda_z|$ via equation (55)), we conclude that the upward propagating secondary GWs at 5–26 UT continue to propagate upward at $z = 46–50$ km, and that they must have a significant meridional propagation direction. Note that having a significant meridional propagation direction is not unusual for secondary GWs; indeed, Becker and Vadas (2018) found that the secondary GWs at McMurdo had significant meridional momentum fluxes. In summary, we conclude that the secondary GWs in this fishbone structure are upward propagating above z_{knee} and downward propagating below z_{knee}, as initially assumed, and that these GWs propagate significantly in the meridional direction. Therefore, criterion #8 is satisfied.

Because all eight criteria are satisfied, it is very likely that the GWs in the fishbone structure on 18 June 2014 are secondary GWs from a horizontally displaced body force.

Finally, we explore how differences in the scaled amplitudes below and above z_{knee} can be used with $\bar{U}$ and $\bar{V}$ to infer the propagation direction of the secondary GWs to within 180°. As discussed previously, the scaled secondary GW amplitudes in Figure 15d are ~1.5–2 times larger above than below z_{knee}, especially at 5–12 UT and 20–26 UT. This could have occurred if a portion of the downward propagating secondary GWs were attenuated by a strong background wind shear because of decreasing $|\lambda_z|$. (For example, if $|c_H - U_H|$ decreases, a GW is more susceptible to convective instability (see section 1 and equation (55)). From Figures 17a and 17b, 5–12 and 20–26 UT correspond to times when $\bar{V}$ was southward. Thus, if the downward propagating secondary GWs were propagating southward, some would have been attenuated during that time. This would not have occurred at 12–20 UT when $\bar{V}$ was northward. Therefore, we conclude that the secondary GWs in the fishbone structure were propagating southward on 18 June 2014.

4.2. Case 2: 29 June 2011

The second case we analyze is on 29 June 2011. Figures 18a and 18b show the corresponding scaled temperature perturbations. From Figure 18b, we see that a possible fishbone structure with $z_{knee} \simeq 52$ km occurs for 10–25 UT at $z = 45–65$ km. We choose $z_{knee} = 52$ km to satisfy criterion #1. We now investigate if these GWs are part of a fishbone structure having $z_{knee} = 52$ km. The removed GWs are shown in Figure 18c. Below the knee, these GWs have large amplitudes and propagate upward until being severely damped at $z \simeq 43–45$ km; additionally, $|\lambda_z|$ does not become extremely large near z_{knee} for these GWs. Above z_{knee}, the GWs have small amplitudes. Therefore, criteria #2–4 are met. Figure 18d shows the derived secondary GWs. The fishbone structure is easily seen. Although $|\lambda_z|$ and τ_r are similar below and above z_{knee}, the scaled amplitudes are smaller below z_{knee}.

We now determine the parameters of the secondary and removed GWs. We define the structure extent to be $t = 10–22$ UT and $z = 45–60$ km. Figure 19 shows the PSD below and above z_{knee} separately for the derived

Table 2
Parameters of the GWs on 29 June 2011

	Below knee		Above knee	
GW type	τ_r (hr)	$\lvert\lambda_z\rvert$ (km)	τ_r (hr)	$\lvert\lambda_z\rvert$ (km)
Secondary GWs	6.10 ± 0.64	6.28 ± 0.83	7.96 ± 0.63	8.10 ± 1.04
Removed GW#1	4.89 ± 0.54	9.93 ± 1.52	3.44 ± 0.52	20.27 ± 6.99
Removed GW#2	10.07 ± 0.79	38.91 ± 17.08		

Note. GWs = gravity waves.

secondary and removed GWs. A single large peak occurs in Figures 19a–19c. A large peak ("GW #1") and a somewhat smaller peak ("GW #2") occur in Figure 19d, implying that there are two upward propagating primary GW packets from below. From Table 2, the secondary GW parameters above z_{knee} have $\tau_r = 7.96 \pm 0.63$ hr and $|\lambda_z| = 8.10 \pm 1.04$ km. In contrast, the removed GW parameters below z_{knee} have $\tau_r = 4.89 \pm 0.54$ hr and $|\lambda_z| = 9.93 \pm 1.52$ km (GW #1) and $\tau_r = 10.07 \pm 0.79$ hr and $|\lambda_z| = 38.91 \pm 17.08$ km (GW #2). Because τ_r are quite different for the secondary GWs and removed GW #1, and because $|\lambda_z|$ are quite different for the secondary GWs and removed GW #2, criterion #5 is satisfied. Additionally, the secondary GW parameters below z_{knee} have $\tau_r = 6.10 \pm 0.64$ hr and $|\lambda_z| = 6.28 \pm 0.83$ km. In contrast, the removed GW parameters above z_{knee} have $\tau_r = 3.44 \pm 0.52$ hr and $|\lambda_z| = 20.27 \pm 6.99$ km. Because τ_r and $|\lambda_z|$ are quite different, criterion #6 is satisfied (i.e., that the secondary GWs below z_{knee} are not continuations of the removed GWs). Finally, for the secondary GW values in Table 2, the peak τ_r and $|\lambda_z|$ below and above z_{knee} are similar. Additionally, from Figure 18d, the scaled GW amplitudes below and above z_{knee} are (1.0–2.0) and (1.0–4.0) $\sqrt{\text{kg/m}^3}$, respectively. Although the variation in the scaled amplitudes is large, the scaled amplitudes below and above z_{knee} are within a factor of 2 of each other. Therefore, criterion #7 is satisfied.

We now check the assumption that the GWs in the fishbone structure with upward (downward) phase progression below (above) z_{knee} are downward (upward) propagating. From Figures 17c and 17d, the wind is northeastward. Using Table 2, equation (61), and $\tau_B = 5.0$ min from MERRA-2, the secondary GWs have $c_{lH} = 21$ and 27 m/s below and above z_{knee}, respectively. From Figures 17c and 17d, $\bar{U}$ and $\bar{V}$ are both less than 21 m/s below z_{knee} in the structure extent. Above z_{knee} at $z \sim 52$–60 km, $\bar{V} < 20$ m/s. However, $\bar{U} < 27$ m/s only at $z \sim 52$–55 km. Above 55 km, $\bar{U} \geq 27$ m/s. Therefore, the GWs in the fishbone structure with upward phase progression below z_{knee} are downward propagating, and the GWs with downward phase progression above z_{knee} at $z = 52$–55 km are upward propagating. Because the slope of the GW phase lines do not change significantly at $z = 55$ km in Figure 18d, which would occur if the upward propagating secondary GWs were propagating zonally, we conclude that the upward propagating secondary GWs have a significant meridional component of their propagation direction, and that they continue to propagate upward at $z = 55$ km. Thus, criterion #8 is satisfied.

Because all eight criteria are satisfied, it is very likely that the GWs in the fishbone structure on 29 June 2011 are secondary GWs from a horizontally displaced body force.

Finally, we explore how the propagation direction of the secondary GWs can be inferred to within 180° via analyzing the difference in their scaled amplitudes below and above z_{knee}. As stated previously, the scaled amplitudes of the downward propagating secondary GWs are a factor of ~2 smaller than that of the upward propagating secondary GWs. From Figure 17d, as the secondary GWs propagate downward (upward), they meet smaller (larger) northward winds. Since c_{lH} is small, a significant portion of the downward secondary GWs would be eliminated if they propagated southward. Therefore, the smaller scaled amplitudes for the downward propagating secondary GWs is consistent with the MERRA-2 winds if the secondary GWs propagated southward.

5. Conclusions and Discussion

In this paper, we reviewed the compressible, linear solutions describing the excitation of secondary GWs from a horizontal body force in an isothermal atmosphere with a constant wind (in altitude and time). Such a body force is created, for example, when primary GWs dissipate and deposit their momentum into the atmosphere. The resulting imbalance of the mean flow generates secondary GWs that have horizontal wavelengths, λ_H,

much larger than that of the primary GWs. These (larger-scale) secondary GWs are therefore different from the small-scale secondary GWs created directly by GW breaking and nonlinear interactions.

We determined the secondary GWs excited by a few idealized body forces. The secondary GWs propagate upward and downward, and in and against the force direction. Horizontal slices of the temperature and velocity perturbations show partial concentric rings that are maximum in and against the force direction. These rings are asymmetric about a line perpendicular to the force direction.

We also found that secondary GWs create fishbone or ">" structures in z-t plots if the body force is horizontally displaced and if the perturbations are scaled by $\sqrt{\bar{\rho}}$. These structure are visible in any horizontal direction except perpendicular to the force direction. The "knee" of the structure, z_{knee}, occurs at the force center. In these structures, the phase lines are asymmetric about $z = z_{\text{knee}}$ (i.e., positive and negative phase lines meet at z_{knee}). Additionally, the GW parameters (τ_{Ir} and $|\lambda_z|$) and the scaled amplitudes are the same below and above z_{knee}. The number of wave cycles in the fishbone structure depends on the ratio of the distance to the force center divided by the force radius. If this ratio is less than a few, the GW phase lines meet at z_{knee}. However, if this ratio is much greater than a few, the GW phase lines do not meet at z_{knee}. These fishbone structures are a general feature of secondary GW generation from local body forces and can be created in the stratosphere, mesosphere, and thermosphere.

We found that the 1-D horizontal and vertical velocity and temperature perturbation spectra for these secondary GWs are quite broad. We also found that these spectra peak at significantly different λ_H, $|\lambda_z|$, τ_{Ir}, and c_{IH}, depending on the duration of the body force, χ, and on the characteristic period of the force, τ_c. (Here τ_c is the period of the assumed dominant secondary GW excited by this force—see equation (53).) For fast forcings with duration $\chi << \tau_c$, $|\widetilde{w'}|^2$ peaks at larger $|\lambda_z|$ and c_{IH} and smaller λ_H and τ_{Ir} than $|\widetilde{u'_H}|^2$ and $|\widetilde{T'/\bar{T}}|^2$. This effect is lessened significantly when $\chi \sim \tau_c$. Additionally, $|\widetilde{u'_H}|^2$ peaks at larger λ_H and τ_{Ir} than $|\widetilde{T'/\bar{T}}|^2$. The fact that $|\widetilde{w'}|^2$, $|\widetilde{u'_H}|^2$ and $|\widetilde{T'/\bar{T}}|^2$ peak at different wave scales occurs because of the GW polarization relations and the fact that the secondary GW spectrum is broad. This is because w' emphasizes the higher-frequency portion of the spectrum, and u'_H and T' emphasize the lower-frequency portion of the spectrum.

We also found that $|\widetilde{w'}|^2$, $|\widetilde{u'_H}|^2$, and $|\widetilde{T'/\bar{T}}|^2$ follow approximate lognormal distributions with respect to λ_H, $|\lambda_z|$, τ_{Ir}, and c_{IH}. This finding is in accordance with lidar observations at McMurdo at $z = 30$–50 km that found that $|\widetilde{T'/\bar{T}}|^2$ followed lognormal distributions with respect to $|\lambda_z|$ and τ_r (Zhao et al., 2017). That, as well as the fact that Zhao et al. (2017) observed GWs with both upward and downward phase progression, suggests that some of the GWs observed at McMurdo at $z = 30$–50 km were likely secondary GWs created in the stratopause region (i.e., $z \sim 40$–65 km) by body forces from primary GW dissipation (Becker & Vadas, 2018). This conclusion is supported by a recent high-resolution wintertime model study at McMurdo using the GW-resolving KMCM (Vadas & Becker, 2018). They found that during strong MW events over McMurdo from downslope winds, MWs propagated to $z \sim 30$–60 km where they broke, dissipated, and excited larger-scale secondary GWs. Thus, they concluded that the GWs at $z = 30$–60 km were a mix of primary and larger-scale secondary GWs. That study also showed that the secondary GWs created fishbone structures in z-t plots.

We then analyzed two wintertime cases at McMurdo where clear fishbone structures were seen in the stratosphere in lidar data: 18 June 2014 and 29 June 2011. For each case, we removed all waves with $\tau_r > 11$ hr, estimated z_{knee}, isolated the GWs in the fishbone structure via selective Fourier filtering below and above z_{knee}, and calculated the PSD. For these cases, the PSD consisted mainly of a single peak below and above z_{knee} having similar peak values of $|\lambda_z|$ and τ_r. We also showed that the upward (downward) phase progression corresponded to downward (upward) propagating GWs via comparison with MERRA-2 winds. We concluded that the GWs in these structures were likely secondary GWs from horizontally displaced body forces, and that they had significant meridional components to their propagation directions. By comparing the asymmetry in the density-scaled amplitudes below and above z_{knee} with the background winds, we showed that both sets of secondary GWs likely propagated southward.

The analysis of these lidar data at McMurdo provides the first direct observational evidence that momentum deposition and subsequent body forcing at McMurdo excites larger-λ_H secondary GWs in the stratopause region that propagate well into the mesosphere. It also shows that the secondary GWs have a wide range of parameters: the derived secondary GWs from this study have ground-based periods of $\tau_r = 6$ to 10 hr and $|\lambda_z| = 6$ to 14 km. Note that the result that secondary GWs have larger λ_H in the mesosphere and lower thermosphere (MLT) is supported by wintertime observations at McMurdo: Zhao et al. (2017) estimated that

the GWs at $z = 30-50$ km had $\lambda_H \sim 350-500$ km, while Chen et al. (2013) and Chen and Chu (2017) estimated that the GWs in the MLT had $\lambda_H \sim 400 - 4,000$ km.

Finally, we note that Kaifler et al. (2017) made observations with a lidar in Finland and saw what may have been a fishbone structure with $z_{\text{knee}} \sim 50$ km on 6 December 2015 (Figure 8 of that work), although they did not identify it as such. They wrote, "Remarkably, upward phase progression waves are found below 50 km and downward phase progression waves above .... Vertical wavelengths of downward and upward phase progression waves at $\sim$ 50 km altitude are in the same range (10-12 km, Figure 8f)". Note from their Figure 8e that the peak periods are also similar for the upward and downward phase progression waves: ~7–8 hr. The authors argue that the upward phase progression waves are downward propagating GWs. We believe that these waves may have been secondary GWs from a horizontally displaced body force centered at $z \sim 50$ km. This body force could have been created by the dissipation of MWs from the Scandinavian Mountains upstream of Finland. Note that the downward GWs could not have been created by wave reflection, because GW reflection occurs when $m \to 0$ or $|\lambda_z| \to \infty$, whereby the phase lines become vertical. This does not appear to occur in the data displayed in that work.

This picture, that primary GWs propagate upward and dissipate, thereby exciting secondary GWs which propagate upward and dissipate, has been previously explored to various extents theoretically and for deep convective plumes (e.g., Vadas & Fritts, 2002; Vadas et al., 2003, 2014; Vadas & Liu, 2009, 2013; Vadas, 2013). Because these secondary GWs have initially small amplitudes and larger λ_H and c_{IH} than the primary GWs, they can propagate to much higher altitudes in the mesosphere and/or thermosphere before dissipating. Upon dissipating, they deposit their momentum and create local body forces, which in turn can excite so-called "tertiary GWs", and so on. This novel picture, that primary GWs propagate upward and dissipate, which excites secondary GWs that propagate upward and dissipate, which excites tertiary GWs that propagate upward and dissipate ... (etc.), has opened a new (and currently unexplored) door in aeronomy that involves complex intertangled coupling processes from the lower atmosphere to the upper thermosphere. The advent of high-resolution, GW-resolving global circulation models now allow for simulations of medium to large-scale primary, secondary, and higher-order GWs using a single global model (e.g., Becker & Vadas, 2018). It is very likely that the generation and dissipation of secondary and higher-order GWs are important dynamical processes in the stratosphere, mesosphere, and thermosphere. Parallel analysis of observational and modeling data will likely result in a much better understanding of the complex coupling processes that GWs facilitate in the Earth's atmosphere.

Acknowledgments
We would like to thank three anonymous reviewers for helpful comments. S. L. V. was supported by the National Science Foundation (NSF) grants PLR-1246405, AGS-1552315, and AGS-1452329. We gratefully acknowledge Zhibin Yu, Brendan R. Roberts, Weichun Fong, and Cao Chen for their excellent winter-over lidar work at McMurdo, Antarctica, from 2011 to 2014. We sincerely appreciate the staff of the United States Antarctic Program, McMurdo Station, Antarctica New Zealand, and Scott Base for their superb support over the years. The McMurdo lidar projects were supported by the NSF grants OPP-0839091, OPP-1246405, and OPP-1443726. E. B. was supported by the Collaborative Research Centre TRR 181 (subproject T1) funded by the German Research Foundation. E. B. would like to thank NCAR/HAO and IAP for the sabbatical opportunity at NCAR/HAO. We thank the Global Modeling and Assimilation Office (GMAO; 2015) for the data from MERRA-2 inst6_3d_ana_Nv: 3d, 6-Hourly, Instantaneous, Model-Level, Analysis, Analyzed Meteorological Fields V5.12.4, Greenbelt, MD, USA, Goddard Earth Sciences Data and Information Services Center (GES DISC; available at https://gmao.gsfc.nasa.gov/reanalysis/MERRA-2/data_{a}ccess/). The model data shown in this paper are available via NWRA's website at https://www.cora.nwra.com/vadas/Vadas_etal_JGR_2018_files/.

References

Abramowitz, M., & Stegun, I. A. (1972). *Handbook of mathematical functions*. New York: Dover Publications.

Alexander, S. P., Klekociuk, A. R., & Murphy, D. J. (2011). Rayleigh lidar observations of gravity wave activity in the winter upper stratosphere and lower mesosphere above Davis, Antarctica (69°S, 78°E). *Journal of Geophysical Research*, *116*, D13109. https://doi.org/10.1029/2010JD015164

Bacmeister, J. T., & Schoeberl, M. R. (1989). Breakdown of vertically propagating two-dimensional gravity waves forced by orography. *Journal of the Atmospheric Sciences*, *46*, 2109–2134.

Becker, E. (2009). Sensitivity of the upper mesosphere to the Lorenz energy cycle of the troposphere. *Journal of the Atmospheric Sciences*, *66*, 647–666. https://doi.org/10.1175/2008JAS2735.1

Becker, E. (2017). Mean-flow effects of thermal tides in the mesosphere and lower thermosphere. *Journal of the Atmospheric Sciences*, *74*, 2043–2063. https://doi.org/10.1175/JAS-D-16-0194.1

Becker, E., Knöpfel, R., & Lübken, F.-J. (2015). Dynamically induced hemispheric differences in the seasonal cycle of the summer polar mesopause. *Journal of Atmospheric and Solar-Terrestrial Physics*, *129*, 128–141. https://doi.org/10.1016/j.jastp.2015.04.014

Becker, E., & Vadas, S. L. (2018). Secondary gravity waves in the winter mesosphere: Results from a high-resolution global circulation model. *Journal of Geophysical Research: Atmospheres*, *123*, 2605–2627. https://doi.org/10.1002/ 2017JD027460

Bossert, K., Kruse, C. G., Heale, C. J., Fritts, D. C., Williams, B. P., Snively, J. B., et al. (2017). Secondary gravity wave generation over New Zealand during the DEEPWAVE campaign. *Journal of Geophysical Research: Atmospheres*, *122*, 7834–7850. https://doi.org/10.1002/2016JD026079

Chen, C., & Chu, X. (2017). Two-dimensional Morlet wavelet transform and its application to wave recognition methodology of automatically extracting two-dimensional wave packets from lidar observations in Antarctica. *Journal of Atmospheric and Solar-Terrestrial Physics*, *162*, 28–47. https://doi.org/10.1016/j.jastp.2016.10.016

Chen, C., Chu, X., McDonald, A. J., Vadas, S. L., Yu, Z., Fong, W., & Lu, X. (2013). Inertia-gravity waves in Antarctica: A case study using simultaneous lidar and radar measurements at McMurdo/Scott Base (77.8°S, 166.7°E). *Journal of Geophysical Research: Atmospheres*, *118*, 2794–2808. https://doi.org/10.1002/jgrd.50318

Chu, X., Huang, W., Fong, W., Yu, Z., Wang, Z., Smith, J. A., & Gardner, C. S. (2011). First lidar observations of polar mesospheric clouds and Fe temperatures at McMurdo (77.8°S, 166.7°E), Antarctica. *Geophysical Research Letters*, *38*, L16810. https://doi.org/10.1029/2011GL048373

Chu, X., Pan, W., Papen, G. C., Gardner, C. S., & Gelbwachs, J. A. (2002). Fe Boltzmann temperature lidar: Design, error analysis, and initial results at the North and South Poles. *Applied Optics*, *41*(21), 4400–4410. https://doi.org/10.1364/AO.41.004400

Chu, X., Yamashita, C., Espy, P. J., Nott, G. J., Jensen, E. J., Liu, H.-L., et al. (2009). Responses of polar mesospheric cloud brightness to stratospheric gravity waves at the South Pole and Rothera, Antarctica. *Journal of Atmospheric and Solar-Terrestrial Physics*, *71*, 434–445. https://doi.org/10.1016/j.jastp.2008.10.002

Chu, X., Yu, Z., Gardner, C. S., Chen, C., & Fong, W. (2011). Lidar observations of neutral Fe layers and fast gravity waves in the thermosphere (110–155 km) at McMurdo (77.8°S, 166.7°E), Antarctica. *Geophysical Research Letters*, *38*, L23807. https://doi.org/10.1029/2011GL050016

Chun, H.-Y., & Kim, Y.-H. (2008). Secondary waves generated by breaking of convective gravity waves in the mesosphere and their influence in the wave momentum flux. *Journal of Geophysical Research*, *113*, D23107. https://doi.org/10.1029/2008JD009792

Dörnbrack, A., Gisinger, S., & Kaifler, B. (2017). On the interpretation of gravity wave measurements by ground-based lidars. *Atmosphere*, *8*, 49. https://doi.org/10.3390/atmos8030049

Dunkerton, T. J. (1978). On the mean meridional mass motions of the stratosphere and mesosphere. *Journal of the Atmospheric Sciences*, *35*, 2325–2333.

Eckermann, S., & Marks, C. (1996). An idealized ray model of gravity wave-tidal interactions. *Journal of Geophysical Research*, *101*(D16), 21,195–21,212. https://doi.org/10.1029/96JD01660

Fong, W., Lu, X., Chu, X., Fuller-Rowell, T. J., Yu, Z., Roberts, B. R., et al. (2014). Winter temperature tides from 30 to 110 km at McMurdo (77.8°S, 166.7°E), Antarctica: Lidar observations and comparisons with WAM. *Journal of Geophysical Research: Atmospheres*, *119*, 2846–2863. https://doi.org/10.1002/2013JD020784

Franke, P. M., & Robinson, W. A. (1999). Nonlinear behavior in the propagation of atmospheric gravity waves. *Journal of the Atmospheric Sciences*, *56*, 3010–3027.

Fritts, D. C., & Alexander, M. J. (2003). Gravity wave dynamics and effects in the middle atmosphere. *Reviews of Geophysics*, *41*, 1003. https://doi.org/10.1029/2001RG000106

Fritts, D. C., Vadas, S. L., Wan, K., & Werne, J. A. (2006). Mean and variable forcing of the middle atmosphere by gravity waves. *Journal of Atmospheric and Solar-Terrestrial Physics*, *68*, 247–265.

Hines, C. O. (1960). Internal atmospheric gravity waves at ionospheric heights. *Canadian Journal de Physique*, *38*, 1441–1481.

Kaifler, N., Kaifler, B., Ehard, B., Gisinger, S., Dörnbrack, A., Rapp, M., et al. (2017). Observational indications of downward-propagating gravity waves in middle atmosphere lidar data. *Journal of Atmospheric and Solar-Terrestrial Physics*, *162*, 16–27. https://doi.org/10.1016/j.jastp.2017.03.003

Kaifler, B., Lübken, F.-J., Höffner, J., Morris, R. J., & Viehl, T. P. (2015). Lidar observations of gravity wave activity in the middle atmosphere over Davis (69°S, 78°E), Antarctica. *Journal of Geophysical Research: Atmospheres*, *120*, 4506–4521. https://doi.org/10.1002/2014JD022879

Klekociuk, A., Lambert, M., Vincent, R., & Dowdy, A. (2003). First year of Rayleigh lidar measurements of middle atmosphere temperatures above Davis, Antarctica. *Advances in Space Research*, *32*(5), 771–776. https://doi.org/10.1016/S0273-1177(03)00421-6

Lighthill, J. (1978). *Waves in fluids*, pp. 504. Cambridge: Cambridge University Press.

Lu, X., Chu, X., Chen, C., Nguyen, V., & Smith, A. K. (2017). First observations of short-period eastward propagating planetary waves from the stratosphere to the lower thermosphere (110 km) in winter Antarctica. *Geophysical Research Letters*, *44*, 10,744–10,753. https://doi.org/10.1002/2017GL075641

Lu, X., Chu, X., Fong, W., Chen, C., Yu, Z., Roberts, B. R., & McDonald, A. J. (2015). Vertical evolution of potential energy density and vertical wave number spectrum of Antarctic gravity waves from 35 to 105 km at McMurdo (77.8°S, 166.7°E). *Journal of Geophysical Research: Atmospheres*, *120*, 2719–2737. https://doi.org/10.1002/2014JD022751

Lu, X., Chu, X., Fuller-Rowell, T., Chang, L., Fong, W., & Yu, Z. (2013). Eastward propagating planetary waves with periods of 1–5 days in the winter Antarctic stratosphere as revealed by MERRA and lidar. *Journal of Geophysical Research: Atmospheres*, *118*, 9565–9578. https://doi.org/10.1002/jgrd.50717

Marks, C. J., & Eckermann, S. D. (1995). A three-dimensional nonhydrostatic ray-tracing model for gravity waves: Formulation and preliminary results for the middle atmosphere. *Journal of the Atmospheric Sciences*, *52*, 1959–1984.

Picone, J. M., Hedin, A. E., Drob, D. P., & Aikin, A. C. (2002). NRLMSISE-00 empirical model of the atmosphere: Statistical comparisons and scientific issues. *Journal of Geophysical Research*, *107*(A12), 1468. https://doi.org/10.1029/2002JA009430

Satomura, T., & Sato, K. (1999). Secondary generation of gravity waves associated with the breaking of mountain waves. *Journal of the Atmospheric Sciences*, *56*, 3847–3858.

Senf, F., & Achatz, U. (2011). On the impact of middle-atmosphere thermal tides on the propagation and dissipation of gravity waves. *Journal of Geophysical Research*, *116*, D24110. https://doi.org/10.1029/2011JD015794

Vadas, S. L. (2007). Horizontal and vertical propagation and dissipation of gravity waves in the thermosphere from lower atmospheric and thermospheric sources. *Journal of Geophysical Research*, *112*, A06305. https://doi.org/10.1029/ 2006JA011845

Vadas, S. L. (2013). Compressible f-plane solutions to body forces, heatings, and coolings, and application to the primary and secondary gravity waves generated by a deep convective plume. *Journal of Geophysical Research: Space Physics*, *118*, 2377–2397. https://doi.org/10.1002/jgra.50163

Vadas, S. L., & Becker, E. (2018). Numerical modeling of the excitation, propagation, and dissipation of primary and secondary gravity waves during wintertime at McMurdo Station in the Antarctic. *Journal of Geophysical Research: Atmospheres*, *123*. https://doi.org/10.1029/2017JD027974

Vadas, S. L., & Fritts, D. C. (2001). Gravity wave radiation and mean responses to local body forces in the atmosphere. *Journal of the Atmospheric Sciences*, *58*, 2249–2279.

Vadas, S. L., & Fritts, D. C. (2002). The importance of spatial variability in the generation of secondary gravity waves from local body forces. *Geophysical Research Letters*, *29*(20), 1984. https://doi.org/10.1029/2002GL015574

Vadas, S. L., & Fritts, D. C. (2013). Corrigendum. *Journal of the Atmospheric Sciences*, *70*, 2680. https://doi.org/10.1175/JAS-D-13-057.1

Vadas, S. L., Fritts, D. C., & Alexander, M. J. (2003). Mechanism for the generation of secondary waves in wave breaking regions. *Journal of the Atmospheric Sciences*, *60*, 194–214.

Vadas, S. L., & Liu, H.-L. (2009). The generation of large-scale gravity waves and neutral winds in the thermosphere from the dissipation of convectively-generated gravity waves. *Journal of Geophysical Research*, *114*, A10310. https://doi.org/10.1029/2009JA014108

Vadas, S. L., & Liu, H.-L. (2013). Numerical modeling of the large-scale neutral and plasma responses to the body forces created by the dissipation of gravity waves from 6 h of deep convection in Brazil. *Journal of Geophysical Research: Space Physics*, *118*, 2593–2617. https://doi.org/10.1002/jgra.50249

Vadas, S. L., Liu, H.-L., & Lieberman, R. S. (2014). Numerical modeling of the global changes to the thermosphere and ionosphere from the dissipation of gravity waves from deep convection. *Journal of Geophysical Research: Space Physics*, *119*, 7762–7793. https://doi.org/10.1002/2014JA020280

Vadas, S. L., Yue, J., She, C.-Y., Stamus, P. A., & Liu, A. (2009). A model study of the effects of winds on concentric rings of gravity waves from a convective plume near Fort Collins on 11 May 2004. *Journal of Geophysical Research*, *114*, D06103. https://doi.org/10.1029/2008JD010753

Watanabe, S., Sato, K., & Takahashi, M. (2006). A general circulation model study of orographic gravity waves over Antarctica excited by katabatic winds. *Journal of Geophysical Research*, *111*, D18104. https://doi.org/10.1029/ 2005JD006851

Wilson, R., Chanin, M. L., & Hauchecorne, A. (1991). Gravity waves in the middle atmosphere observed by Rayleigh lidar, 1. Case studies. *Journal of Geophysical Research*, *96*(D3), 5153 – 5167. https://doi.org/10.1029/90JD0223

Yamashita, C., Chu, X., Liu, H.-L., Espy, P. J., Nott, G. J., & Huang, W. (2009). Stratospheric gravity wave characteristics and seasonal variations observed by lidar at the South Pole and Rothera, Antarctica. *Journal of Geophysical Research*, *114*, D12101. https://doi.org/10.1029/2008JD011472

Zhao, J., Chu, X., Chen, C., Lu, X., Fong, W., Yu, Z., et al. (2017). Lidar observations of stratospheric gravity waves from 2011 to 2015 at McMurdo (77.84°S, 166.69°E), Antarctica: Part I. Vertical wavelengths, periods, and frequency and vertical wavenumber spectra. *Journal of Geophysical Research: Atmospheres*, *122*, 5041 – 5062. https://doi.org/10.1002/2016JD026368

Zhou, X., Holton, J. R., & Mullendore, G. L. (2002). Forcing of secondary waves by breaking of gravity waves in the mesosphere. *Journal of Geophysical Research*, *107*(D7), 4058. https://doi.org/10.1029/2001JD001204